International Journal of Nanomedicine

Dovepress
Taylor & Francis Group

Open Access Full Text Article

ORIGINAL RESEARCH

Protective Effects of GalNac-Modified Red Blood Cell-Derived Extracellular Vesicles Against Liver Diseases

Xiaofang Huang[1,2], Jie Yang[3], Yuanyuan Hu[1], Shuai Li[1], Zhijian Cai[4,5,*], Chen Li[1,*], Weidong Qin[1,2,*], Gensheng Zhang[3,6,*]

[1]Department of Critical Care Medicine, Qilu Hospital of Shandong University, Jinan, Shandong, People's Republic of China; [2]Key Laboratory of Cardiovascular Remodeling and Function Research, Chinese Ministry of Education, Chinese Ministry of Health and Chinese Academy of Medical Sciences, Qilu Hospital of Shandong University, Jinan, Shandong, People's Republic of China; [3]Department of Critical Care Medicine, Second Affiliated Hospital of Zhejiang University School of Medicine, Hangzhou, Zhejiang, People's Republic of China; [4]Institute of Immunology, Zhejiang University School of Medicine, Hangzhou, Zhejiang, People's Republic of China; [5]Department of Orthopedics, The Second Affiliated Hospital of Zhejiang University School of Medicine, Hangzhou, Zhejiang, People's Republic of China; [6]Key Laboratory of Multiple Organ Failure (Zhejiang University), Ministry of Education, Hangzhou, Zhejiang, People's Republic of China

*These authors contributed equally to this work

Correspondence: Gensheng Zhang, Department of Critical Care Medicine, Second Affiliated Hospital of Zhejiang University School of Medicine, 88 Jiefang Road, Hangzhou, 310009, People's Republic of China, Email genshengzhang@zju.edu.cn

Objective: The high morbidity and mortality of liver diseases warrant the development of more effective therapeutic methods. Extracellular vesicles (EVs) are optimal drug delivery vehicles, albeit with insufficient targeting specificity. The aim of this study was to develop modified red blood cell-derived EVs (RBC-EVs) for targeted drug delivery into hepatocytes, and verify their therapeutic efficacy in animal models of acute liver failure (ALF), non-alcoholic fatty liver disease (NAFLD) and hepatocellular carcinoma (HCC).

Methods: RBC-EVs were extracted and modified with triantennary N-acetyl galactosamine sequences (GalNac-RBC-EVs), then loaded with drugs or oligonucleotides. The GalNac-RBC-EVs uptake by hepatocytes was monitored both in vitro and in vivo. Models of ALF, NAFLD and HCC were established using C57BL/6J mice. RBC-EVs/GalNac-miR-155-ASO was prepared for the treatment of ALF by anchoring GalNac-miR-155-ASO to RBC-EVs. GalNac-RBC-EVs loaded with PJ34 (GalNac-RBC-EVs/PJ34) were used for treating NAFLD. Finally, GalNac-Rab7-siRNA and PJ34 were co-loaded into RBC-EVs (RBC-EVs/GalNac-Rab7-siRNA/PJ34) as a therapeutic agent for HCC. The therapeutic efficacy, biosafety and stability of the modified RBC-EVs were analyzed as per standard protocols.

Results: GalNac-RBC-EVs exhibited higher hepatocyte accumulation via asialoglycoprotein receptor (ASGPR)-mediated uptake both in vivo and in vitro. In ALF, RBC-EVs/GalNac-miR-155-ASO reduced inflammation through suppression of pyroptosis ($P<0.0001$), apoptosis ($P<0.0001$), and mitigation of necroptosis ($P<0.0001$). For NAFLD/HCC treatment, GalNac-RBC-EVs/PJ34 decreased hepatic triglyceride ($P<0.0001$) and attenuated HCC growth ($P<0.001$) via PARP-1 inhibition ($P<0.0001$). Co-delivery of GalNac-Rab7-siRNA enhanced PJ34 efficacy ($P<0.0001$) by prolonging drug retention. No significant toxicity was observed in vital organs (ALT/AST levels, $P>0.05$; histopathology scores, $P>0.05$).

Conclusion: Drug-loaded GalNac-RBC-EVs selectively targeted the hepatocytes, and displayed significant therapeutic efficacy in ALF, NAFLD or HCC without any side effects. Altogether, RBC-EVs modified with GalNac are a promising drug carrier for the effective and precise treatment of various liver diseases.

Keywords: red blood cells, extracellular vesicles, GalNac, ASGPR, hepatocytes

Introduction

Liver diseases, such as virus infections, alcoholic liver disease, non-alcoholic fatty liver disease (NAFLD), are characterized by hepatocyte injury and inflammation that lead to the development of cirrhosis and liver cancer. They are serious public health concerns due to high global prevalence and poor long-term clinical outcomes.[1] Hepatocytes are

Received: 9 January 2025
Accepted: 30 May 2025
Published: 15 July 2025

Graphical Abstract

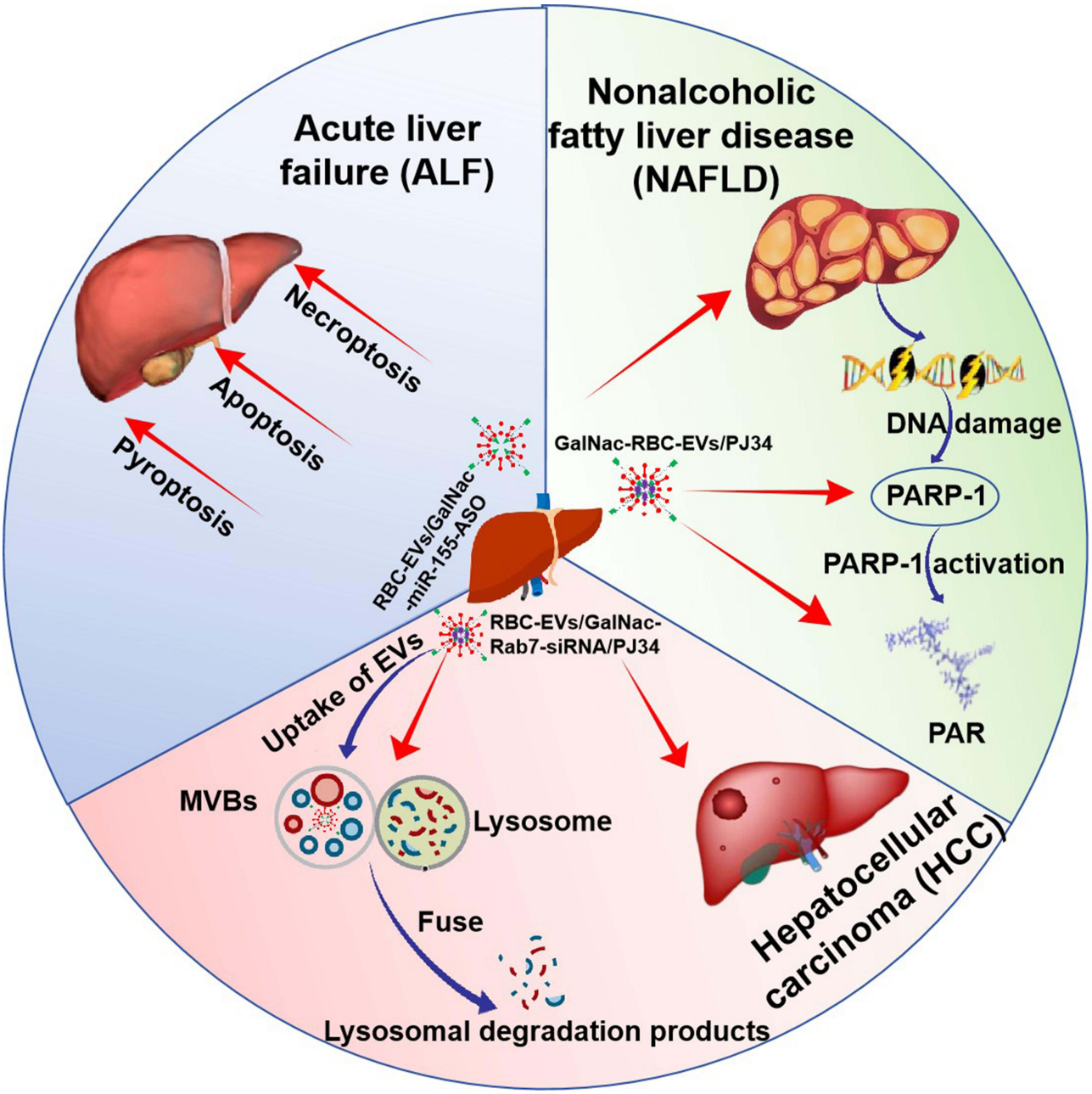

the major parenchymal cells in the liver, they play a pivotal role in various biochemical and metabolic functions including immune cell activation, lipid and protein metabolism, and detoxification, distinguishing them from non-parenchymal supportive cells such as Kupffer cells and hepatic stellate cells (HSCs). It is widely accepted that hepatocytes are not only the active drivers in liver inflammation but also the direct target of injury,[2] resulting in hepatocyte death which identified as a typical pathological feature in liver diseases. Acute liver failure (ALF) is a life-threatening disease characterized by extensive hepatocyte death, and can evolve over days or weeks to a lethal outcome.[3] NAFLD is the most common cause of liver diseases, and is characterized by excessive accumulation of triglycerides in the hepatocytes due to increased inflow of free fatty acids, as well as de novo hepatic lipogenesis.[4] Hepatocellular

carcinoma (HCC) ranks the third among all cancers in terms of mortality rates, and accounts for 8.3% of all cancer-related deaths worldwide. Currently, targeted therapies for advanced HCC are severely limited.[5] Due to the complex etiology and heterogeneity of liver diseases, most drugs have sub-optimal efficacy. Given that the pathological changes in the liver specifically affect the hepatocytes, it is crucial to devise strategies for the targeted delivery of drugs to these cells in order to improve treatment outcomes.

miR-155 is a key regulator of macrophage polarization, driving M1 pro-inflammatory phenotype and promoting cytokine production.[6] Given miR-155's central role in mediating hepatic inflammation and metabolic dysregulation, antisense oligonucleotide (ASO) targeting miR-155 is a logical strategy to reduce inflammation and restore lipid homeostasis.[7] PARP-1, the most abundant member of the PARP family (contributing >90% of total PARP activity), is overactivated in NAFLD and HCC.[8–10] This hyperactivation leads to excessive NAD^+ consumption, disrupting fatty acid oxidation and exacerbating hepatic steatosis.[8] Moreover, PARP-1-mediated poly(ADP-ribosyl)ation (PARylation) has been implicated in the stabilization of oncogenic factors, which drives lipid metabolism reprogramming and immune evasion in HCC.[11] PJ34 selectively inhibits PARP-1 enzymatic activity, preventing excessive DNA damage repair and reducing NAD^+ depletion. This alleviates fatty acid oxidation impairment and oxidative stress.[12] In HCC, the therapeutic potential of PARP inhibition is further substantiated by preclinical evidence indicating that PJ34 can attenuate tumor growth through synergistic interactions with DNA-damaging agents or by targeting the PARP1/CD36 axis, which is essential for the survival of HCC cells and the modulation of the immune microenvironment,[11] making it a viable target for therapeutic intervention.

To implement precision medicine, several novel targeted delivery platforms are under development, such as lipid nucleic acid nanoparticles (LNP), N-acetylgalactosamine (GalNac) conjugates, extracellular vesicles (EVs), and virus-like particle (VLP).[13] Unlike viral vectors, these novel targeted delivery systems are nanocarriers with extremely low cytotoxicity and immunogenicity, and can also decrease the accumulation of drugs in non-target organs, resulting in lower off-target toxicity.[14] The asialoglycoprotein receptor (ASGPR), a lysosomal-targeting receptor highly expressed on hepatocytes, has emerged as a key mediator of liver-specific drug delivery.[15] ASGPR binds with high affinity to GalNac, a ligand that can be chemically conjugated to oligonucleotides (eg, siRNA, antisense RNAs) or nanocarriers to enable hepatocyte-targeted delivery via receptor-mediated endocytosis.[16] Over 30 clinical trials are underway using GalNac-conjugated siRNA for various clinical indications.[17] However, challenges remain in optimizing delivery efficiency: naked GalNac-siRNA conjugates often exhibit limited endosomal escape and rapid renal clearance, resulting in suboptimal target knockdown.[18,19] EVs, a group of heterogeneous nanosized cell-derived vesicles,[20] mediate cell-to-cell communication by transporting active biomolecules from the producer cells to the recipient cells.[21] EVs not only can deliver nucleic acids but also can deliver proteins and small chemical drugs. As the natural delivery tool, red blood cell-derived EVs (RBC-EVs) eliminates the need for in vitro cell culture, and the production of RBC-EVs can be easily scaled-up, which is advantageous for potential clinical applications. Importantly, unlike other cell types that contain a nucleus with DNA, RBC-EVs devoid of introducing foreign genetic material or causing unpredictable effects.[22,23] This characteristic ensures that RBC-EVs possess many more favorable properties than other EVs.

In this study, we aimed to develop a hepatocyte-specific targeted delivery strategy with GalNac-tethered RBC-EVs to broaden the therapeutic potential of combination therapy. We hypothesized that the modified GalNac-RBC-EVs would selectively target hepatocytes and deliver ASO or siRNA via the ASGPR/GalNac pathway. Additionally, in conjunction with siRNA, the RBC-EVs would also transport the chemical drug PJ34 to the hepatocytes, thereby integrating two therapeutic modalities into a single nanoplatform. This novel combined delivery system is anticipated to achieve significant therapeutic effects in mouse models of ALF, NAFLD and HCC.

Materials and Methods

Separation and Identification of EVs

All procedures involving human participants were approved by the Ethics Committee of Qilu Hospital, Shandong University (Jinan, Shandong, China, KYLL-202310-037) and complied with the Declaration of Helsinki, blood was obtained from 20 healthy donors with the O serotype prior to sample collection. Written informed consent documentation was signed by all study participants. The samples (75 mL per donor) were collected into 10 mL purple-top EDTA

anticoagulant tubes at room temperature, and centrifuged at 3000 g for 15 min and passed through a leukodepletion filter (Terumo Imugard® III, Tokyo, Japan) to separate the RBCs. The RBC-EVs were isolated as previously described.[23] Briefly, the RBCs were diluted in PBS and incubated overnight with 1 μM calcium ionophore (Sigma-Aldrich, MO, USA) at 37°C to induce eryptosis. The solution was sequentially centrifuged at 600 g for 20 min, 1600 g for 15 min, 3260 g for 15 min and 10,000 g for 30 min at 4°C to remove the debris, and the supernatant was ultracentrifuged with a SW32Ti rotor (Beckman Coulter, CA, USA) at 100,000 g for 70 min at 4°C. The pelleted EVs were resuspended in PBS and analyzed further. For transmission electron microscopy (TEM) analysis, EVs were fixed on a 200-mesh carbon-coated copper grids. After washing with PBS, EVs were chemically stained with 4% (w/v) uranyl acetate (Sigma-Aldrich) for 60 seconds at room temperature (25°C), and images were captured using Talos L120C G2 electron microscope (Thermo Scientific, USA). The size and number of EVs were assessed using a NanoSight NS300 equipped with a 405 nm laser (Malvern, Great Malvern, UK). Videos (60 s duration, 30 frames/s) were recorded and particle movement was analyzed using the nanoparticle tracking analysis (NTA) software (NanoSight version 2.3, UK). The expression of the EV markers, tumor susceptibility gene 101 (TSG101), apoptosis linked gene 2 interacting protein X (Alix), Stomatin (STOM), hemoglobin (HBA) and the negative marker Calnexin, were analyzed by Western blotting.

Western Blotting

Proteins extracted from cells/tissues were quantified using a BCA Protein Assay Kit (#P0012S, Beyotime Biotechnology, Nantong, China). Equal amounts of protein per sample (10 μg) were separated by 10% SDS-polyacrylamide gel (Thermo Fisher Scientific) electrophoresis, and transferred to PVDF membranes (Millipore). After blocking with 5% non-fat milk for 1 h at room temperature, the proteins were incubated overnight with primary antibodies at 4°C, and then with secondary antibodies at room temperature for 1 h. The positive bands were visualized using a luminescent image analyzer (Amersham Imager 600, GE, MA, USA), and quantified using ImageJ software (NIH, USA). The antibodies and the corresponding dilutions are listed in Table S1.

Preparation of GalNac-Decorated RBC-EVs

RBC-EVs were incubated with cholesterol-modified GalNac-miR-negative control (NC) (GalNac-RBC-EVs), GalNac-miR-155-ASO (RBC-EVs/GalNac-miR-155-ASO), or GalNac-siRNA-Rab7 (RBC-EVs/GalNac-Rab7-siRNA) at 37°C for 30 min. The sequences for miR-155-ASO, miR-NC and siRNA-Rab7 are listed in Table S2. PJ34 was incorporated into GalNac-RBC-EVs or RBC-EVs/GalNac-siRNA-Rab7 by electroporation using a BTX electroporator (Harvard Biosciences, Cambridge, MA, USA) at 350 V,150 μF and a pulse duration of 10 ms in 0.2 cm electroporation cuvettes. The loading efficiency of PJ34 was quantified by high-performance liquid chromatography (HPLC), and its concentration in GalNac-RBC-EVs/PJ34 or RBC-EVs/GalNac-siRNA-Rab7/PJ34 was determined by LC-MS/MS. The loading efficiency of GalNac-siRNA-Rab7 was determined using the mass-gray value standard curve. The entrapment efficiency was calculated as follows: Entrapment Efficiency (%) = (Measured Fluorescence/Standard Fluorescence)×100. The cholesterol-modified GalNac sequences including GalNac-miR-155-ASO, GalNac-miR-NC and GalNac-siRNA-Rab7 were all synthesized by Quanyang Biotech Co., Ltd. (Quanyang Biotech, Guangzhou, China).

Flow Cytometry

To verify successful GalNac modification, flow cytometry was employed. EVs (5 μg) were absorbed onto 4% w/v 4 μm aldehyde/sulfate latex beads (Invitrogen, CA, USA, #A37304,) for 20 min, and then blocked with EV-free fetal bovine serum (FBS) at room temperature for 30 min. The beads were washed twice with PBS at 3000 g for 5 min, and incubated with antibodies for 30 min at 4°C. After washing twice with PBS, the beads were acquired on the ACEA NovoCyte flow cytometer, and the fluorescence intensities were analyzed using the FlowJo software (Tree Star, USA).

Additionally, flow cytometry was used to assess EV uptake by specific cells. Cells were seeded in 6-well plates at the density of 5×10^5 cells/well, stimulated as appropriate, and harvested. After washing once, the cells were incubated with fluorochrome-labeled antibodies or IgG isotype control (BioLegend, CA, USA) in 100 μL FACS buffer for 30 min at 4°C in the dark. The cells were centrifuged at 1500 rpm for 5 min at 4°C, and resuspended in 200 μL FACS buffer. The cells were acquired on the ACEA NovoCyte flow cytometer, and the fluorescence intensities were analyzed using the FlowJo software (Tree Star, USA).

Animal Models

The animal experiments were approved by the Animal Care and Use Committee of Qilu Hospital of Shandong University (Jinan, Shandong, China, KYLL-2022(ZM)-001). The Animal Welfare and Ethics Committee of the hospital reviewed and approved all protocols, ensuring compliance with their operational guidelines for anesthesia, postoperative care, and euthanasia by CO_2 inhalation. C57BL/6J mice (6–8 weeks old, Charles Rivers, Beijing, China) were housed in a specific pathogen-free animal care facility on a 12 h light/dark cycle, with full access to standard mouse chow and water.

For the ALF model, the mice were injected intravenously with RBC-EVs/GalNac-miR-155-ASO (5 mg/kg≈0.64 OD) or GalNac-miR-155-ASO (0.64 OD), and intraperitoneally injected with 10 μg/kg LPS (Sigma-Aldrich, St Louis, MO, USA) and 400 mg/kg D-GalN (Sigma-Aldrich) in a total volume of 0.1 mL per mouse 24 h later.[24,25] After 6 h, the mice were sacrificed under anesthesia with an intraperitoneal injection of 0.8% pentobarbital sodium (60 mg/kg, n=8). Blood samples were taken from the right aorta, and the plasma fraction was centrifuged at 3000 rpm for 10 min and analyzed within 2 h. The tissues were harvested, and a portion was fixed in formalin for histological assessment, and the remainder was snap frozen in liquid nitrogen and stored at −80°C for further analysis.

To induce NAFLD, six-weeks-old male mice were fed a methionine-choline-deficient (MCD) diet (Product Code: TP36225MCD, Trophic Animal Feed High-tech Co., Ltd., Jiangsu, China) containing 10% fat, 70% carbohydrates, and 20% protein, with methionine and choline reduced to <0.1% and 0.01% respectively for 12 weeks. Mice fed with normal control diet (NCD) were used as the control group. The HFD-fed mice were randomly divided into the PJ34 (10 mg/kg), RBC-EV/PJ34 (5 mg/kg≈250 μg/kg PJ34) and GalNac-RBC-EVs/PJ34 (5 mg/kg≈250 μg/kg PJ34) groups (n=8) and injected intravenously with the respective formulations every three days from the 4 weeks.

To establish the HCC model, six-weeks-old female C57BL/6J mice were subcutaneously inoculated with Hepa1-6 cells (1×10^7 cells/each) into the right flanks after 1 week of acclimatization. Once the tumors grew to approximately 150 mm^3, the mice were administered intravenous injections every three days according to the following treatment groups (n=8): control (DMSO), PJ34 (10 mg/kg), RBC-EV/PJ34 (5 mg/kg), GalNac-RBC-EVs/PJ34 (5 mg/kg) and RBC-EV/GalNac-Rab7-siRNA /PJ34 (5 mg/kg). Body weight and tumor size were measured every three days. The mice were anesthetized with an intraperitoneal injection of 0.8% pentobarbital sodium prior to euthanasia after 28 days, and the tumor tissues and primary organs were harvested, weighed and stored at −80°C for future analysis.

Isolation of Primary Liver Cells

Primary hepatocytes, Kupffer cells and hepatic stellate cells (HSCs) were isolated from C57BL/6J mice. The mice were anaesthetized with pentobarbital sodium, and the liver was perfused with Hank's balanced salt solution buffer (pH 7.4, Gibco #14175095) via the vena cava. Hepatocytes, Kupffer cells and HSCs were isolated as described previously.[25–27] Briefly, the liver was sequentially perfused with collagenase perfusion, differential centrifugation, and density gradient purification. For hepatocytes, the supernatant was centrifuged at 50 g for 3 min. For Kupffer cells isolation, the supernatant was washed at 500 g for 8 min. The collected pellet was resuspended in 30% and 60% Percoll and centrifuged at 800 g for 20 min. For HSCs, the supernatant was centrifuged at 1400 g for 20 min. Lastly, the interface enriched with hepatocytes, Kupffer cells or HSCs cells was aspirated and washed twice with Dulbecco's modified Eagle medium (DMEM). The isolated cells were seeded on collagen-coated 6-well culture plates and used for experiments the following day.

Cell Culture and Stimulation

HepG2 (HB-8065) and Hep1-6 (CRL-1830) cells were purchased from the American Type Culture Collection (ATCC). BEL7402 was purchased from Scientific Laboratories of Southern Medical University (Guangzhou, Guangdong, China). All experiments were conducted with cells between passage 5 and passage 15 to ensure phenotypic stability. HepG2, BEL7402 and Hep1-6 cells were maintained in DMEM supplemented with 10% (V/V) FBS (Biological Industries, Beit Haemek, Israel), 100 U/mL penicillin and 100 μg/mL streptomycin. Alpha mouse liver 12 (AML12) cell was obtained from ATCC (CRT-2254) and cultured in DMEM/F-12 supplemented with 10% FBS, 100 U/mL penicillin, 100 μg /mL streptomycin, 5 μg/mL ITS premix and 40 ng/mL dexamethasone in a humidified incubator at 37°C with 5% CO_2. The AML12 cells were seeded at approximately 70% confluence in complete growth medium, and treated with 100 ng/mL

tumor necrosis factor-α (TNF-α) and 44 μg/mL D-GalN for 12 h. The stimulated cells were treated with GalNac-RBC-EVs (5 μg) or RBC-EVs/GalNac-miR-155-ASO (5 μg) for 48 h. In another experiment, Hepa1-6 cells were plated in 12-well plates at the density of 4×10^5 cells/well, and then treated with GalNac-RBC-EVs (5 μg) or RBC-EVs/GalNac-Rab7-siRNA (5 μg) for 48 h. The efficacy of siRNA-mediated knockdown of Rab7 was evaluated by Western blotting.

In Vitro Uptake of EVs

EVs were labeled with 2 μM PKH26 (Sigma-Aldrich, #MINI26) in Diluent C for 10 min at room temperature, followed by quenching with 1% BSA and two washes in PBS/0.1% BSA via ultracentrifugation (100,000 g, 1 h). The cells were incubated with the PKH26-labeled EVs under normal culture conditions for 5 min. After washing twice with PBS, the cells were analyzed by flow cytometry or fixed with 4% paraformaldehyde (Beyotime, Nantong, China) for immunostaining. Images were taken under a confocal laser scanning microscope.

Biochemical Assays

Blood was centrifuged at 1500 g for 10 min to collect clear serum and analysed within 2h. Serum levels of alanine transaminase (ALT) and aspartate aminotransferase (AST) were measured using specific assay kits (Jiancheng, Nanjing, Jiangsu, China). The serum levels of TNF-α, interleukin-1β (IL-1β) and IL-6 were measured using specific ELISA kits (Thermo Fisher Scientific #88-7324-88, #88-7013A-88, #88-7064-88) according to the manufacturer's instructions. OD values were read at 450 nm on a BioTek Synergy H1. Intra- and inter-assay CVs were <10% and <15%, respectively.

Immunofluorescence

The liver tissues were cryo-embedded in Tissue-Tek Cryo-O.C.T. Compound (Thermo Fisher Scientific) by submerging the embedding mold in liquid nitrogen-chilled isopentane (−50°C) for 10~15 seconds, followed by storage at −80°C. Sections (5 μm) were cut on a Leica CM1950 cryostat (−20°C). The tissue sections were stained overnight with primary antibodies at 4°C, followed by the corresponding fluorescence-labelled secondary antibodies at room temperature for 1 h. After counterstaining with DAPI for 20 min at room temperature, the sections were observed with a Nikon A1R confocal microscope (Nikon). The antibodies and the corresponding dilutions are listed in Table S1.

Histopathological Analysis

The mice were euthanized and exsanguinated by perfusing with saline. The tissues were harvested and fixed in 4% paraformaldehyde for 48 h, embedded in paraffin, and cut into 4 μm-thick sections. Hematoxylin and eosin (H&E) staining was performed as per standard protocols, and the slides were observed under a microscope for morphological assessment. The samples were histologically scored in a double-blind manner method as described previously.[28] Histopathological scoring of acute liver injury was performed using a modified Suzuki system,[29] evaluating four parameters: hepatocellular necrosis, inflammatory infiltration, steatosis, and hemorrhage/sinusoidal congestion. The severity of tissue damage in each sample was graded from 0 to 3 (0 = normal; 1 = mild; 2 = moderate; and 3 = severe), and the total score was calculated.

Oil Red O (ORO) Staining

Fixed frozen sections were washed with distilled water, and excess water was drained by rinsing twice with 100% propylene glycol. The sections were stained with 0.5% ORO in 60% propylene glycol for 7 min at 60°C, destained with 85% propylene glycol for 5–10 seconds under microscopic monitoring, and counterstained with hematoxylin. After rinsing thoroughly with water, the sections were mounted with aqueous mounting media and observed under an epifluorescence microscope.

Quantitative Real-Time PCR

Total RNA was extracted from the cells and tissues using TRIzol reagent (Invitrogen) and transcribed to cDNA using the ExScript reverse transcription-PCR (RT-PCR) kit (TaKaRa BIO, Shiga, Japan). QRT-PCR was performed in the Mx3000P 160 Real-Time PCR System (Agilent Technologies) with the SYBR Premix Ex TaqTM kit (#RR420A, Takara Bio Inc., Japan) following the manufacturer's instructions. Gene expression was normalized to two endogenous

controls (*GAPDH* and *U6*), and relative mRNA or miRNA levels were calculated with the $2^{-\Delta\Delta Ct}$ method. The primer sequences are listed in Table S2.

Immunohistochemistry

Mice tissue sections were routinely deparaffinized and rehydrated, and heated in 10 mM sodium citrate buffer (pH 6) for antigen retrieval. After blocking with 5% BSA, the slides were incubated overnight with primary antibodies at 4°C, followed by the corresponding HRP-conjugated secondary antibodies at room temperature for 30 min. The sections were washed thrice with PBS, and staining was developed using 3,3′-diaminobenzidine tetrahydrochloride (DAKO, Copenhagen, Denmark). Images were randomly captured and analyzed using ImageJ software (NIH, USA), and the number of positively stained cells were counted and normalized to the total number of cells. The antibodies are listed in Table S1.

Cell Counting Kit 8 (CCK-8) Assay

Cells were seeded into 96-well plates at the density of 1×10^4 cells per well and treated with 100 ng/mL TNF-α and 44 μg/mL D-GalN. After 18 h, RBC-EVs loaded with GalNac-NC (5 μg) or GalNac-miR-155-ASOs (5 μg) were added, and the cells were incubated for 48 h. The viability of the cells was analyzed using the CCK-8 kit (#CK04, Dojindo Molecular Technologies, Kyushu, Japan) according to the manufacturer's instructions. The absorbance (A) was measured at 450 nm using a microplate reader (Bio-Tek, Winooski, VT, USA).

TUNEL Assay

Liver tissues were fixed overnight in 4% paraformaldehyde, dehydrated, embedded in paraffin, and cut into thin sections. TUNEL assay was performed to detect apoptotic cells according to the manufacturer's instructions (#G3250, Promega Corporation, WI, USA). The number of TUNEL+ cells were counted in 5 random fields at 200× magnification under a fluorescence microscope (Zeiss, Germany).

Annexin V Binding Assay

Apoptosis was detected using an FITC Annexin V apoptosis detection kit (#556547, BD Biosciences, NJ, USA) according to the manufacturer's instructions. Briefly, cells stimulated with apoptotic reagents were harvested and resuspended in 1 × binding buffer (1×10^6 cells/mL). Aliquots of 10^5 cells (100 μL) were incubated with 5 μL annexin V and 5 μL propidium iodide (PI) at room temperature for 15 min in the dark. The cells were analyzed by flow cytometry (FACSVerse, BD Biosciences, NJ, USA) using FACSuite software (BD Biosciences).

Colony Formation Assay

Cells were seeded in 6-well plates at the density of 500 cells/well and treated with DMSO, PJ34 (0.05 μg), RBC-EV/PJ34 (1 μg), GalNac-RBC-EVs/PJ34 (1 μg) and RBC-EV/GalNac-Rab7-siRNA/PJ34 (1 μg). The medium was changed every two days for 14 days, and the colonies were fixed with methyl alcohol and stained with 5% Giemsa solution (#GS500, Sigma-Aldrich, pH 6.8) for 15 min, and rinsed thoroughly. Colonies (>50 cells, diameter >50 μm) were manually counted under a light microscope and validated by ImageJ analysis (NIH, Bethesda, MD, USA).[30]

In vivo Tracking of RBC-EVs

GalNac-RBC-EVs (5 mg/kg) or RBC-EVs/GalNac-Rab7-siRNA (5 mg/kg) were labelled with VivoTrack 680 (Fluorescence, Beijing, China), PKH26 (Sigma-Aldrich) or carboxyfluorescein succinimidylester (CFSE, Thermo Fisher Scientific) according to the manufacturer's instructions. For the labeling of VivoTrack 680, a mixture was prepared consisting of 100 μg of EVs in 200 μL of PBS with 42 μM VivoTrack 680. This mixture was incubated at 25°C for 30 minutes. The staining process was terminated by the addition of an equal volume of exosome-depleted FBS, followed by an additional incubation for 1 minute. Subsequently, unbound dye was eliminated through ultracentrifugation at 120,000 g for 90 minutes. The labelled EVs were injected into C57BL/6J mice via the tail vein. The mice were sacrificed 24 h later, and the brain, heart, lungs, liver, spleen, kidneys and gut were collected and imaged by an in vivo imaging system (IVIS, PerkinElmer, Waltham, MA, USA) to track the uptake of labeled EVs.

Statistical Analysis

GraphPad Prism 8.0 (GraphPad Software Inc., San Diego, CA, USA) was used for all statistical analyses. All data were expressed as the mean ± standard deviation. For normally distributed data, the mean differences between two groups were compared by unpaired Student's *t*-test, and multiple groups were compared by ANOVA and Newman-Keuls test. For data with non-normal distribution, non-parametric Kruskal–Wallis *H*-test was used for comparison. P value <0.05 was considered statistically significant.

Results

GalNac-RBC-EVs Specifically Targeted the Hepatocytes by Binding to ASGPR

RBC-EVs were separated and identified as previously described.[23] TEM analysis showed the typical bilayer membrane structure of the EVs (Figure 1A). According to NTA, the mean diameter of the EVs was 144.4 ± 48.0 nm (Figure 1B). Furthermore, the purified EVs expressed the characteristic marker proteins including TSG101 and Alix, as well as STOM and HGB1, the major RBC protein (Figure 1C). Notably, RBC-EVs were negative for expression of the Calnexin protein, an endoplasmic reticulum marker that was common in many cell types but absent in RBCs. These data illustrated the characteristics and purity of RBC and its derived EVs, and also enhanced the experimental credibility for the subsequent application of EVs.

The procedure for the synthesis of cholesterol-GalNac-miRNA modified RBC-EVs (GalNac-RBC-EVs) has been illustrated in Figure 1D. We anchored cholesterol-FAM-GalNac-miRNA to the exosomal membrane via co-incubation at 37°C for 30 min, the fluorescence signals of FAM were detected in the PKH26-labeled RBC-EVs (Figure 1E), indicating successful modification of the RBC-EVs with GalNac sequences. To ensure optimal loading of the RBC-EVs with GalNac-miRNA, we adjusted the proportion of RBC-EVs (100 μg) and GalNac-miRNA (0.64 OD) accordingly. TEM analysis indicated that GalNac-RBC-EVs did not compromise the structural integrity of the double concave discs (Figure S1A). Furthermore, NTA verified that the particle sizes of GalNac-RBC-EVs were comparable to those of RBC-EVs, measuring 151.2±37.5 nm (Figure S1B).

ASGPR is primarily expressed on the hepatocytes (Figure 1F) and binds to GalNac sequences with high affinity.[31] To determine whether GalNac-RBC-EVs can selectively target the hepatocytes, we incubated primary hepatocytes, Kupffer cells and HSCs with PKH26-labeled GalNac-RBC-EVs. As shown in Figure 1G, the GalNac-RBC-EVs demonstrated a preferential internalization by hepatocytes in comparison to Kupffer cells and HSCs following a 5-minute incubation period. Furthermore, ASGPR expression was observed in HepG2 cells, whereas it was absent in Bel7402 cells (Figure S1C). Correspondingly, HepG2 cells incubated with CFSE-labeled GalNac-RBC-EVs exhibited significantly stronger fluorescence signals (green) than Bel7402 cells (Figure S1D). To further confirm the targeting capability of GalNac-RBC-EVs towards hepatocytes in vivo, C57BL/6J mice were administered with PKH26-labeled GalNac-RBC-EVs. The fluorescence signals of GalNac-RBC-EVs were more pronounced in the hepatocytes ($ASGPR^+$) compared to the Kupffer cells ($F4/80^+$) 24 h after injection ($P<0.0001$, Figure 1H and 1I). Finally, no significant alterations were observed in the fluorescence intensity of FAM-GalNac-RBC-EVs following storage at −80°C for six months (Figure 1J) or after undergoing repeated thaw/freeze cycles (Figure 1K), which confirmed the stability of the modified RBC-EVs. Altogether, RBC-EVs conjugated with GalNac sequences were stable and selectively taken up by the hepatocytes rather than Kupffer cells.

RBC-EVs/GalNac-miR-155-ASO Alleviated Acute Liver Injury in Mice

In our previous study, we found that GalNac-miR-155-ASO protected mice against ALF.[32] However, its effect was weaker than that of RBC-EVs/miR-155-ASO, which can be partly attributed to the rapid degradation of the exposed miRNA by RNases. In this study, miR-155 expression was significantly elevated in the hepatocytes of the untreated ALF model mice ($P<0.0001$), and RBC-EVs/GalNac-miR-155-ASO downregulated miR-155 to a greater extent compared to GalNac-miR-155-ASO ($P<0.001$, Figure 2A). Furthermore, miR-155 expression in the Kupffer cells was also lower in the RBC-EVs/GalNac-miR-155-ASO group compared to that in the GalNac-miR-155-ASO group, although this difference did not reach statistical significance ($P=0.24$, Figure S2A). To further comprehend this result, we stimulated the hepatocytes and Kupffer cells with TNF-α and D-GalN, and then treated the hepatocytes with GalNac-miR-155-ASO and co-cultured them with Kupffer cells for 48 h (Figure S2B). The co-cultured Kupffer cells showed a relative lower miR-

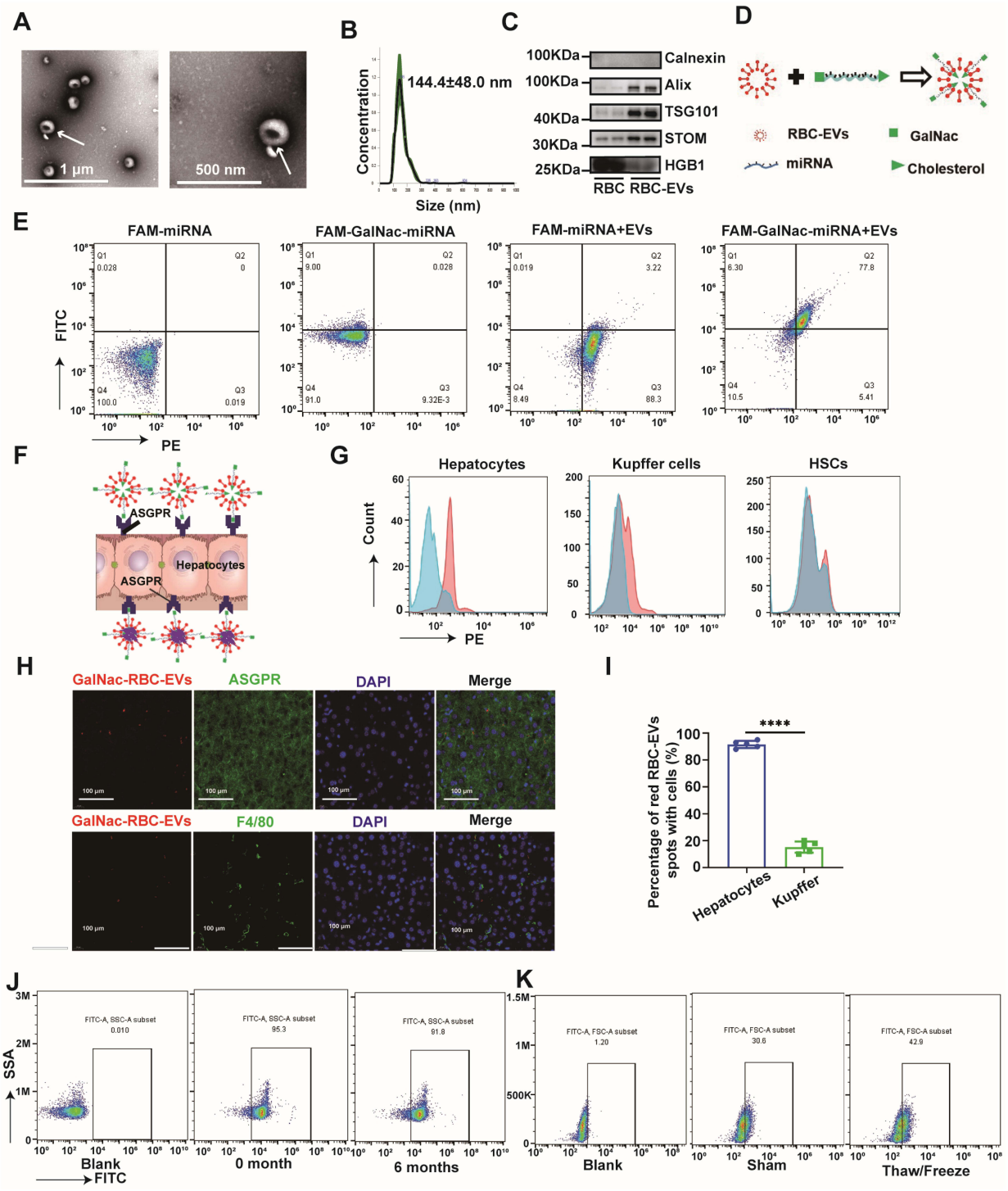

Figure 1 GalNac-modified RBC-EVs specifically targeted hepatocytes by binding to ASGPR. (**A**) Representative transmission electron microscopy (TEM) images of RBC-EVs. Scale bars: 1 μm and 500 nm. (**B**) Size distribution of RBC-EVs as measured by nanoparticle tracking analysis (NTA). (**C**) Immunoblot showing the expression of marker proteins in RBC-EVs and RBCs. (**D**) Schematic diagram showing the synthesis of RBC-EVs with cholesterol-modified GalNac-miRNA. (**E**) FAM-miRNA or cholesterol modified FAM-GalNac-miRNA was co-incubated with RBC-EVs for 30 min at 37°C. Flow cytometry plots show the binding of cholesterol-modified GalNac-miRNA with RBC-EVs (GalNac-RBC-EVs). (**F**) Schematic representation of GalNac-RBC-EVs binding to ASGPR on the hepatocytes. (**G**) Hepatocytes, Kupffer cells and hepatic stellate cells (HSCs) were isolated from the liver of C57BL/6J mice, and incubated with GalNac-RBC-EVs at 37°C for 5 min. The flow cytometry plots show uptake of RBC-EVs /GalNac-miRNA into the hepatocytes, Kupffer cells and HSCs. (**H**) GalNac-RBC-EVs (5 mg/kg) stained with PKH26 were intravenously injected into C57BL/6J mice, and the liver tissues were analyzed by immunofluorescence 24 h later. Representative images show the uptake of PKH26-labeled GalNac-RBC-EVs (red) by hepatocytes (ASGPR, green) or Kupffer cells (F4/80, green). (**I**) The percentage of hepatocytes (ASGPR) or Kupffer cells (F4/80) with PKH26-labeled GalNac-RBC-EVs. (**J**) Flow cytometry plots showing the fluorescence intensity of FAM-GalNac-RBC-EVs after storage at −80°C for 6 months. (**K**) Flow cytometry plots showing the fluorescence intensity of FAM-GalNac-RBC-EVs after repeated thaw and freeze cycles. **P* <0.05, ***P* <0.01, ****P* <0.001 and *****P* <0.0001 (one-way ANOVA test; mean ± SD).
Abbreviation: ns, not significant.

https://doi.org/10.2147/IJN.S510937

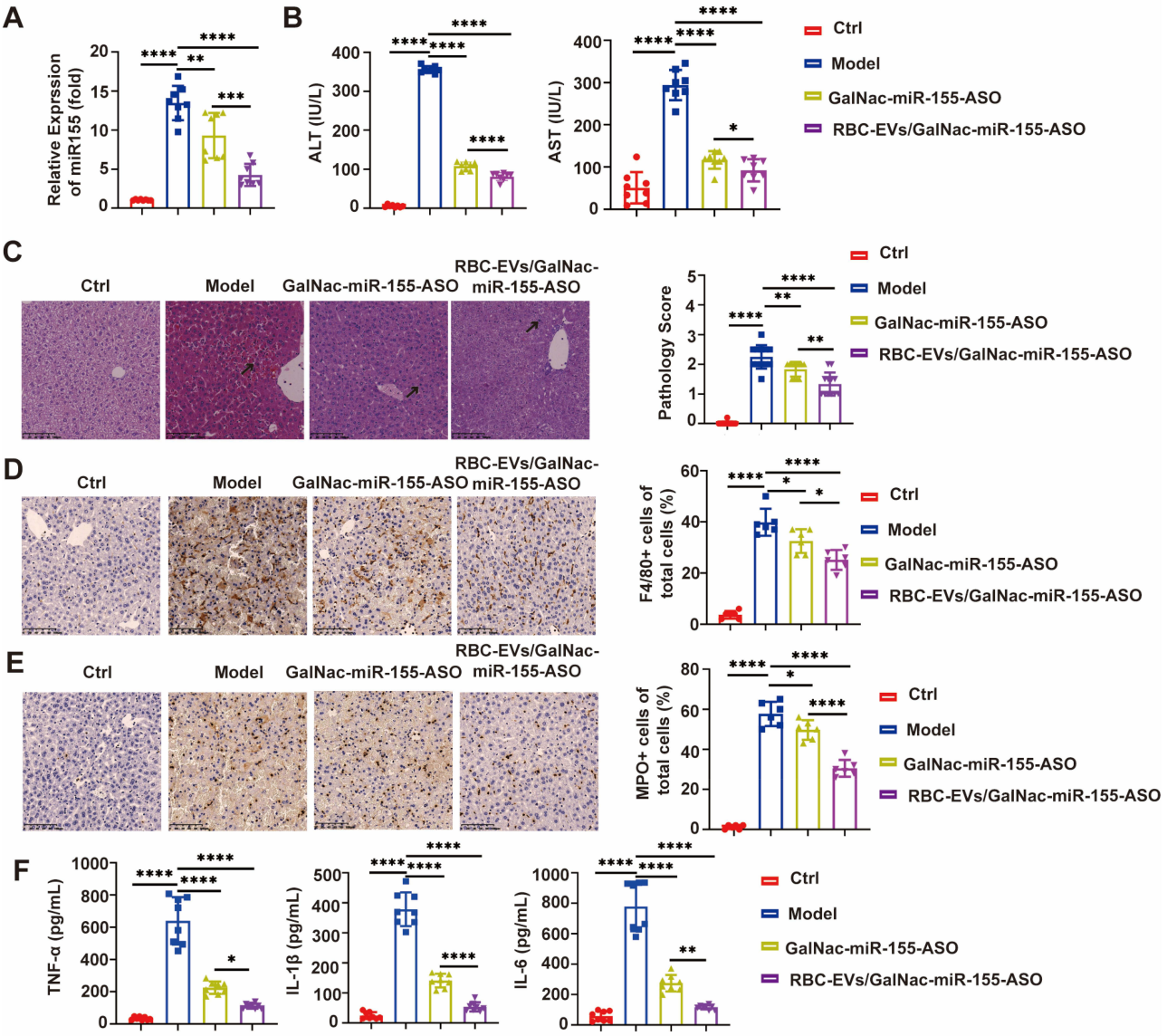

Figure 2 RBC-EVs/GalNac-miR155-ASO inhibited hepatic inflammation and alleviated ALF in mice. ALF was induced in six-weeks-old male C57BL/6J mice using D-GalN/LPS, and the mice were intravenously injected with GalNac-miR-155-ASO (0.64 OD) or RBC-EVs/GalNac-miR-155-ASO (5 mg/kg). The control (Ctrl) group was injected with PBS. (**A**) The relative expression of miR-155 in the indicated groups as measured by qRT-PCR (n=8). (**B**) Serum AST and ALT levels in the indicated groups as measured by ELISA (n=8). (**C**) Representative images of H&E-stained liver tissues and the histological scores in the indicated groups. Scale bars, 100 μm. Arrows for lesion. (**D**) Representative images of liver tissues from the indicated groups showing F4/80$^+$ cells. The percentage of F/480$^+$ cells was analyzed. Scale bars, 100 μm. (**E**) Representative images of liver tissues from the indicated groups showing MPO$^+$ cells. The percentage of MPO$^+$ cells was analyzed. Scale bars, 100 μm. (**F**) Serum levels of TNF-α, IL-1β and IL-6 in the indicated groups as measured by ELISA (n=8). *P <0.05, **P <0.01, ***P <0.001 and ****P <0.0001 (one-way ANOVA test; mean ± SD).
Abbreviations: ALT, alanine transaminase; AST, aspartate aminotransferase; ns, not significant.

155 expression compared to the GalNac-miR-NC group (P=0.008), suggesting a cross-effect between hepatocytes and Kupffer cells (Figure S2C). RBC-EVs/GalNac-miR-155-ASO treatment also led to a significant reduction in the serum levels of ALT (P<0.0001) and AST (P<0.0001) in mice with acute liver injury (Figure 2B). The liver tissues from the ALF group showed extensive edema, inflammatory damage and necrosis compared to the liver from healthy control mice (P<0.0001). Both GalNac-miR-155-ASO (P=0.009) and RBC-EVs/GalNac-miR-155-ASO (P<0.0001) improved the pathological scores, and the latter had a more significant effect (P=0.001, Figure 2C). Furthermore, we also detected massive infiltration of F4/80$^+$ macrophages and MPO$^+$ neutrophils in the liver tissues of the ALF group, which was mitigated by RBC-EVs/GalNac-miR-155-ASO (P<0.0001, P<0.0001), and to a lesser extent by GalNac-miR-155-ASO (P=0.02, P=0.03, Figure 2D and E). Consistent with this, the serum levels of TNF-α, IL-1β and IL-6 were consistently

and markedly elevated in the ALF group compared to the control group (all $P<0.0001$), and RBC-EVs/GalNac-miR-155-ASO resulted in a more significant obvious reduction than GalNac-miR-155-ASO ($P=0.03$, $P<0.0001$, $P=0.006$, Figure 2F). Altogether, these results suggested that the therapeutic effects of RBC-EVs/GalNac-miR-155-ASO for ALF was superior to that of GalNac-miR-155-ASO.

RBC-EVs/GalNac-miR-155-ASO Ameliorated ALF in Mice by Inhibiting PANoptosis

Given the critical role of programmed cell death of hepatocytes in ALF, we analyzed the impact of RBC-EVs/GalNac-miR-155-ASO on pyroptosis, apoptosis and necroptosis (PANoptosis) in the hepatocytes. Compared to the control group, ALF increased the expression of the pyroptosis-related proteins GSDME ($P<0.0001$) and NLRP3 ($P<0.0001$). However, RBC-EVs/GalNac-miR-155-ASO significantly downregulated these proteins ($P<0.0001$, $P<0.0001$), and their expression levels were lower compared to that in the GalNac-miR-155-ASO group ($P=0.0004$, $P=0.002$, Figure 3A and B). Furthermore, pro-apoptotic proteins including cleaved-caspase-3 ($P<0.0001$), cleaved-caspase-7 ($P<0.0001$), cleaved-caspase-8 ($P<0.0001$) and Bax ($P<0.0001$) were upregulated, while the anti-apoptotic protein Bcl-2 ($P<0.0001$) was downregulated in the ALF group. GalNac-miR-155-ASO ($P=0.03$, $P=0.004$, $P=0.0001$, $P=0.0005$, $P<0.0001$) and RBC-EVs/GalNac-miR-155-ASO ($P<0.0001$, $P<0.0001$, $P=0.0001$, $P<0.0001$, $P<0.0001$) reduced the expression of the pro-apoptotic proteins in the hepatocytes, and the effect was more significant with the latter ($P<0.0001$, $P<0.0001$, $P=0.99$, $P=0.0003$, $P=0.0002$, Figure 3C and D). Consistent with the above results, ALF markedly increased the percentage of $TUNEL^{+}$ apoptotic cells in the liver ($P<0.0001$), while treatment with GalNac-miR-155-ASO ($P=0.01$) or RBC-EVs /GalNac-miR-155-ASO ($P<0.0001$) decreased the apoptotic rates (Figure 3E and F). Finally, the necroptosis-related p-RIP ($P<0.0001$), p-RIP3 ($P<0.0001$) and p-MLKL ($P<0.0001$) were upregulated in the ALF group relative to the control group. RBC-EVs/GalNac-miR-155-ASO significantly reduced the expression of these proteins compared to GalNac-miR-155-ASO ($P<0.0001$, $P=0.009$, $P<0.0001$, Figure 3G and H). Furthermore, we detected the expression of PANoptosis markers, Z-DNA binding protein 1 (ZBP1), the key switch of PANoptosis. Western blotting showed a significant increase in the expression level of ZBP1 in ALF group compared with the control mice ($P<0.0001$), RBC-EVs/GalNac-miR-155-ASO markedly decreased the expression of ZBP-1 compared with GalNac-miR-155-ASO ($P<0.0001$, Figure 3I). Taken together, RBC-EVs/GalNac-miR-155-ASO protected mice against ALF by suppressing PANoptosis in the hepatocytes.

GalNac-RBC-EVs/PJ34 Inhibited PARP-1 Expression and Activity in the Liver of Mice with NAFLD

Although NAFLD progression involves different hepatic cells, the pathological process is initiated due to aberrant lipid metabolism within the hepatocytes.[33] Various metabolic disorders are associated with elevated oxidative stress and DNA damage, which induce PARP-1 activation.[34] The PARP inhibitor PJ34 has demonstrated therapeutic effects in the murine NAFLD model.[35] EVs have been shown to be promising carriers for small molecule drugs such as doxorubicin and paclitaxel. Therefore, we encapsulated PJ34 in the GalNac-RBC-EVs and evaluated the effect of GalNac-RBC-EVs/PJ34 on PARP-1 expression and activity in the HFD-induced model of NAFLD. TEM analysis indicated that the encapsulation of PJ34 did not compromise the structural integrity of the double concave vesicular discs (Figure 4A). The particle size of GalNac-RBC-EVs/PJ34 was significantly larger than that of RBC-EVs, measuring 188.1 ± 69.7 nm compared to 144.4 ± 48.0 nm ($P = 0.01$; Figure 4B and C). According to the HPLC results, ~5 μg PJ34 was encapsulated into 100 μg RBC-EVs/PJ34 or GalNac-RBC-EVs/PJ34 after electroporation (Figure 4D and Figure S3A). HFD feeding significantly upregulated PARP-1 and PAR (activated PARP-1) in the hepatocytes compared to that in the normal diet-fed control group ($P<0.0001$, $P<0.0001$). However, RBC-EVs/PJ34 (5 mg/kg≈250 μg/kg PJ34) and GalNac-RBC-EVs/PJ34 (5 mg/kg≈250 μg/kg PJ34) decreased PARP-1 expression ($P<0.0001$, $P<0.0001$) and activity ($P<0.0001$, $P<0.0001$), and the effect of GalNac-RBC-EVs/PJ34 was superior to the rest ($P<0.0001$, $P<0.0001$, Figure 4E and F). Taken together, GalNac-RBC-EVs/PJ34 inhibited the NAFLD-related increase in PARP-1 expression and activity in the hepatocytes.

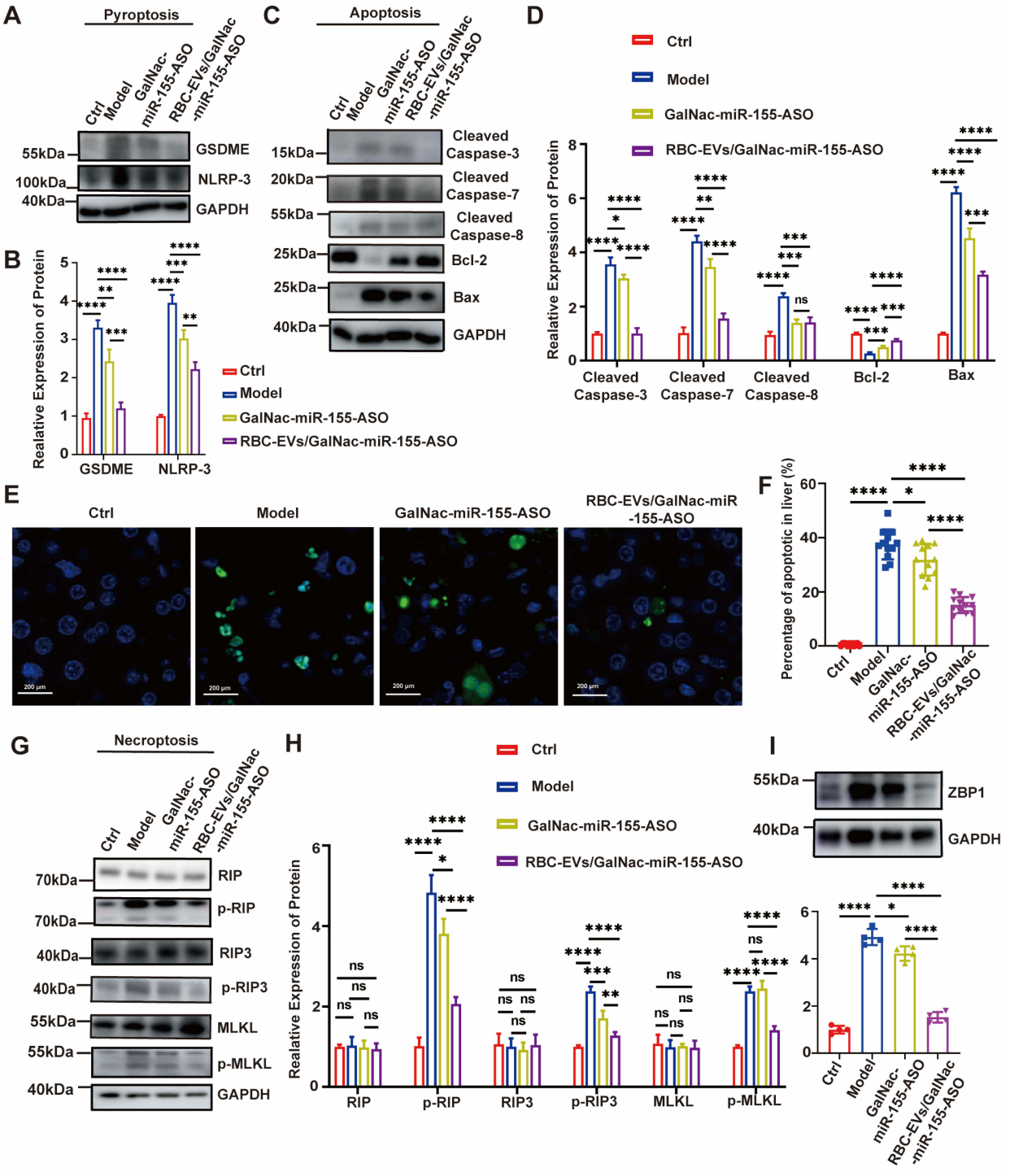

Figure 3 RBC-EV/GalNac-miR155-ASO protected against ALF by inhibiting PANoptosis. ALF was induced in six-weeks-old male C57BL/6J mice using D-GalN/LPS, and the mice were intravenously injected with GalNac-miR-155-ASO (0.64 OD) or RBC-EVs/GalNac-miR-155-ASO (5 mg/kg). The control group (Ctrl) received PBS. Hepatocytes and Kupffer cells were isolated for further analyses. (**A**) Immunoblot showing the expression of GSDME and NLRP3 in the hepatocytes of the indicated groups. GAPDH was used as the internal control. (**B**) Quantification of GSDME and NLRP3 protein expression from three experiments. (**C**) Immunoblot showing the expression of cleaved caspase-3, cleaved caspase-7, cleaved caspase-8, Bcl-2 and Bax in the hepatocytes of the indicated groups. GAPDH was used as the internal control. (**D**) Quantification of apoptosis-related protein expression from three experiments. (**E**) Representative images showing TUNEL-positive apoptotic cells in the liver tissues of the indicated groups. (**F**) The average number of apoptotic cells in the liver tissues calculated from three independent experiments. (**G**) Immunoblot showing the expression of RIP, p-RIP, RIP3, p-RIP3, MLKL and p-MLKL in the hepatocytes of the indicated groups. GAPDH was used as the internal control. (**H**) Quantification of necroptosis-related protein expression from three independent experiments. (**I**) Immunoblot and quantification of the expression of ZBP1 in the hepatocytes of the indicated groups. GAPDH was used as the internal control. **P* <0.05, ***P* <0.01, ****P* <0.001 and *****P* <0.0001 (one-way ANOVA test; mean ± SD).

Abbreviation: ns, not significant.

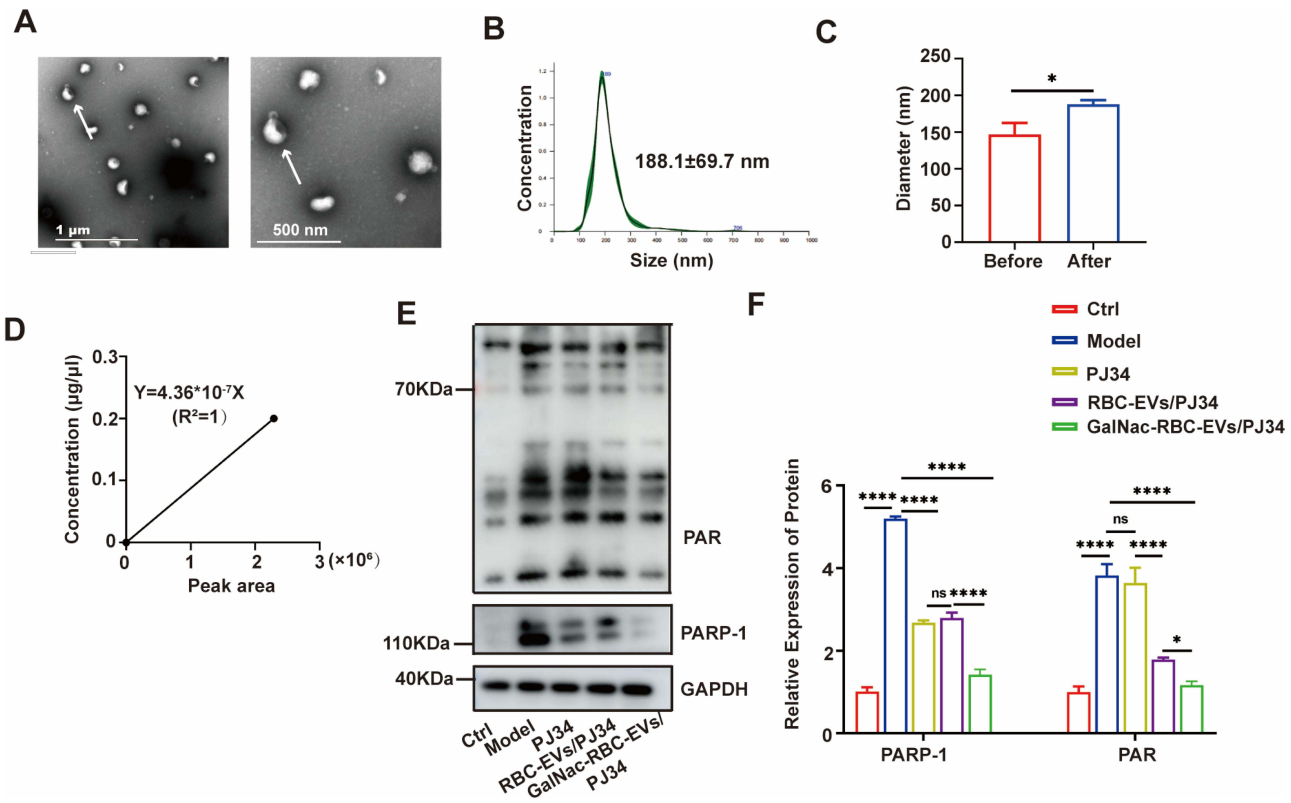

Figure 4 GalNac-RBC-EVs/PJ34 inhibited PARP-1 expression and activity in the NAFLD model. (**A**) Representative TEM images showing morphology of GalNac-RBC-EVs /PJ34. Scale bars, 1 μm and 500 nm. (**B**) Size distribution of GalNac-RBC-EVs/PJ34 as measured by NTA. (**C**) Quantitative analyses on the size of GalNac-RBC-EVs before and after PJ34 loading. (**D**) The amount of PJ34 in RBC-EVs/PJ34 and GalNac-RBC-EVs/PJ34 was quantified by high-performance liquid chromatography (HPLC). Six-weeks-old male C57BL/6J mice were fed HFD for 12 weeks to induce NAFLD (n=8), and treated with PJ34 (10 mg/kg), RBC-EVs/PJ34 (5 mg/kg) and GalNac-RBC-EVs/PJ34 (5 mg/kg) every other day from the 4 weeks. The control group (Ctrl) received PBS. (**E**) Immunoblot showing expression of PARP-1 and PAR in the liver of control, NAFLD, PJ34, RBC-EVs/PJ34 and GalNac-RBC-EVs/PJ34 groups. (**F**) Quantification of PARP-1 and PAR expression from three independent experiments. **P* <0.05, ***P* <0.01, ****P* <0.001 and *****P* <0.0001 (one-way ANOVA test; mean ± SD).
Abbreviation: ns, not significant.

GalNac-RBC-EVs/PJ34 Alleviated the Symptoms of NAFLD

Mice fed with HFD showed decreased body weight gain (P=0.0005) and elevated liver weight (P<0.0001) compared to control group. Mice in the GalNac-RBC-EVs/PJ34 group exhibited an increase in body weight (P=0.62) and a reduction in liver weight (P=0.05) compared to those in the RBC-EVs/PJ34 group; however, the change in body weight did not achieve statistical significance (Figure 5A and B). The serum ALT and AST levels were markedly elevated in the NAFLD group compared to that in the control mice (all P<0.0001), and showed a significant decrease following treatment with GalNac-RBC-EVs/PJ34 (all P<0.0001), while the effect of RBC-EVs/PJ34 was less obvious (Figure 5C). Moreover, NAFLD significantly increased the serum levels of triglycerides (TG), total cholesterol (TC), low-density lipoprotein cholesterol (LDL) and non-esterified fatty acid (NEFA), and decreased that of high-density lipoprotein cholesterol (HDL) (all P<0.0001). Treatment with GalNac-RBC-EVs/PJ34 significantly restored the levels of these metabolites (all P<0.0001). In comparison to the RBC-EVs/PJ34 group, the GalNac-RBC-EVs/PJ34 group exhibited reduced levels of TG, TC, and NEFA (Student-t test, P=0.0006, P=0.04, P=0.04, Figure 5D–F). Histological examination of the liver tissues showed higher fat deposition in the NAFLD group compared to the control group (Figure 5G). Consistent with this, ORO staining showed larger and more abundant lipid droplets in the liver tissues of the NAFLD group compared to that in the control group (P<0.0001, Figure 5H). GalNac-RBC-EVs/PJ34 not only decreased the overall hepatic fat deposition but also attenuated the formation of lipid droplets in the NAFLD mice, and its effects were superior to that of RBC-EVs/PJ34 (all P<0.0001, Figure 5G and H). Furthermore, quantitative analysis demonstrated that the GalNac-RBC-EVs/PJ34 group showed a statistically significant decrease in lipid droplet count (P < 0.001), while there was no significant difference in the mean droplet diameter (P = 0.9) when compared to the model

https://doi.org/10.2147/IJN.S510937

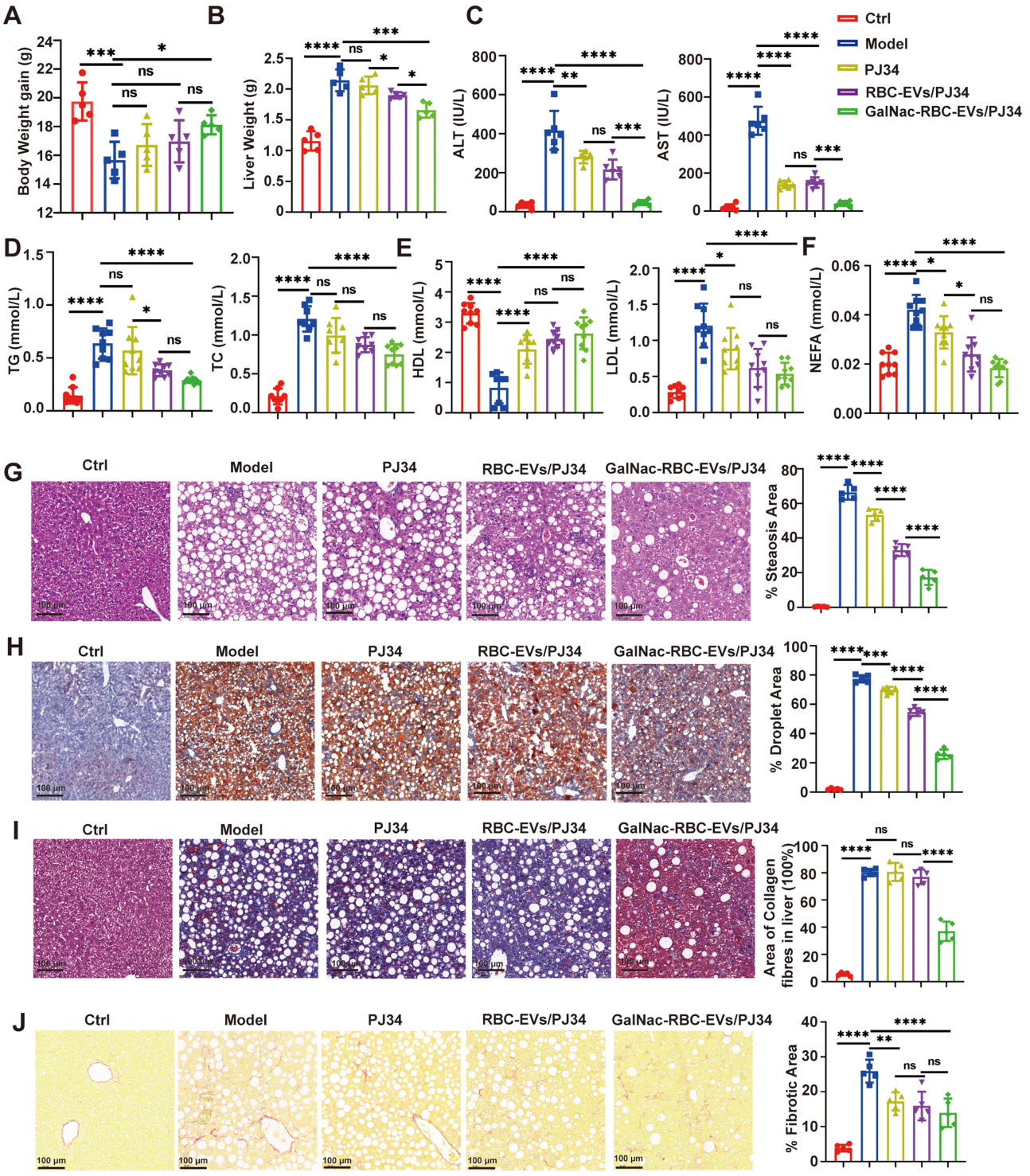

Figure 5 GalNac-RBC-EVs/PJ34 alleviated NAFLD in mice. Six-weeks-old male C57BL/6J mice were fed HFD for 12 weeks, and treated with PJ34 (10 mg/kg), RBC-EVs/PJ34 (5 mg/kg) and GalNac-RBC-EVs/PJ34 (5 mg/kg) every other day from the 4 weeks. The control group (Ctrl) received PBS (n=8). (**A**) Gain in body weight after 12 weeks in the indicated groups (n=8). (**B**) Liver weight in the indicated groups after 12 weeks (n=8). (**C**) Serum ALT and AST levels in the indicated groups (n=8). (**D**) Serum TG and TC levels in the indicated groups (n=8). (**E**) Serum HLD and LDL levels in the indicated groups (n=8). (**F**) Serum NEFA levels in the indicated groups (n=8). (**G**) Representative images of H&E-stained liver tissues of the indicated groups. Scale bars, 100 μm. (**H**) Representative images of ORO-stained frozen liver tissue sections of the indicated groups. Scale bar, 100 μm. (**I**) Representative images and percentage of Masson's trichrome (MT)-stained area (%) with collagen fibers in the liver. Scale bar, 100 μm. (**J**) Representative images and percentage of sirius red-stained area (%) representing collagen fibers in the liver. Scale bar, 100 μm, **P* <0.05, ***P* <0.01, ****P* <0.001 and *****P* <0.0001 (one-way ANOVA test; mean ± SD).

Abbreviations: ALT, alanine transaminase; AST, aspartate aminotransferase; TG, Triglyceride; TC, total cholesterol; HDL, high-density lipoprotein cholesterol; LDL, low-density lipoprotein cholesterol; NEFA, non-esterified fatty acid; ORO, Oil Red O; ns, no significant.

group (Figure S3B). Masson's trichrome (MT) staining showed massive collagen accumulation in the liver of mice with NAFLD, which was reduced by GalNac-RBC-EVs/PJ34, and to a lesser extent by RBC-EVs/PJ34 (all $P<0.0001$, Figure 5I). However, there was no significant difference in the intensity of sirius red staining between the RBC-EVs /PJ34 and GalNac-RBC-EVs/PJ34 groups ($P=0.86$, Figure 5J). Taken together, GalNac-RBC-EVs/PJ34 effectively inhibited NAFLD-induced hepatic steatosis and fibrosis in comparison with RBC-EVs/PJ34 or PJ34.

PJ34-Loaded RBC-EVs/GalNac-Rab7-siRNA Decreased Rab7 and PARP-1 Expression in Hepatocytes Simultaneously

Rab7 plays a critical role in the fusion of multivesicular bodies (MVBs) and lysosomes, and subsequent MVB degradation.[36] Therefore, we hypothesized that inactivation of Rab7 might increase drug concentration in the cells by decreasing MVB degradation. To test our hypothesis and demonstrate the diversity of the GalNac modification, we incorporated GalNac-Rab7-siRNA into the PJ34-loaded RBC-EVs (Figure 6A). TEM analysis showed that GalNac-Rab7 -siRNA and drug encapsulation did not alter the integrity of the double concave vesicular discs (Figure S4A). The particle size of RBC-EVs/GalNac-Rab7-siRNA/PJ34 was larger than that of RBC-EVs ($P = 0.008$, Figure S4B and C). We assessed the entrapment efficiencies of GalNac-Rab7-siRNA utilizing a standard curve methodology (Figure S4D). The entrapment efficiency for GalNac-siRNA was calculated to be 69.5±11.9%. Following this, we investigated the therapeutic potential of RBC-EVs/GalNac-Rab7-siRNA/PJ34. As expected, Rab7 expression was significantly down-regulated in Hepa1-6 cells following incubation with RBC-EVs/GalNac-Rab7-siRNA ($P<0.0001$, Figure 6B), which in turn inhibited the fusion of RBC-EVs (red) with lysosomes (marked with LAMP 1, green) (Figure 6C). To further elucidate the role of Rab7-siRNA in MVB degradation, fluorochrome-labeled PJ34 (green) was incubated with PKH-26 RBC-EVs/GalNac-Rab7-siRNA (red), the immunofluorescence analysis showed that downregulation of Rab7 in Hepa1-6 by RBC-EVs/GalNac-Rab7-siRNA inhibited the fusion of PJ34 with Lamp1 (cyan). Quantitative co-localization analysis revealed that RBC-EVs/GalNac-Rab7-siRNA/PJ34 exhibited significantly reduced LAMP1 association compared to GalNac-RBC-EVs/PJ34 ($P=0.006$) (Figure 6D). Consistent with the above, the cytosolic concentration of PJ34 was higher in Hepa1-6 cells incubated with RBC-EVs/GalNac-Rab7-siRNA/PJ34 compared to that in the GalNac-RBC-EVs /PJ34 group (Figure S4E). To test the effects of RBC-EVs/GalNac-Rab7-siRNA/PJ34 in vivo, we first determined the biodistribution of Vivotrack680-labeled RBC-EVs/PJ34 and GalNac-RBC-EVs/PJ34 in mice bearing Hepa1-6 tumors. The IVIS results showed that both RBC-EVs/PJ34 and GalNac-RBC-EVs/PJ34 accumulated in the liver and tumor tissues 24 h after intravenous injection, and there was no significant difference between the two groups (Figure S4F). Western blotting analysis showed that compared to PJ34, RBC-EVs/PJ34 or GalNac-RBC-EVs/PJ34, RBC-EVs/GalNac-Rab7-siRNA/PJ34 reduced Rab7 expression in the hepatocytes ($P<0.0001$) but not in the Kupffer cells (all $P>0.05$, Figure 6E). In addition, PARP-1 (Figure 6F and S4G) and PAR were both downregulated in the hepatocytes (Figure 6G and S4H) and Kupffer cells (Figure 6H and S4I) of mice treated with RBC-EVs/PJ34, GalNac-RBC-EVs/PJ34 or RBC-EVs/GalNac-Rab7-siRNA/PJ34, and the latter had the optimum effects.

RBC-EVs/GalNac-Rab7-siRNA/PJ34 Suppressed Liver Tumor Progression

Next, we evaluate the therapeutic potential of RBC-EVs/GalNac-Rab7-siRNA/PJ34 against HCC cells in vitro. As shown in Figure 7A, RBC-EVs/GalNac-Rab7-siRNA/PJ34 (1 μg) significantly decreased the viability of Hepa1-6 cells in vitro ($P=0.002$), while PJ34 (0.05 μg), RBC-EVs/PJ34 (1 μg) and GalNac-RBC-EVs/PJ34 (1 μg) had no obvious effects (all $P>0.05$, Figure 7A). Likewise, RBC-EVs/GalNac-Rab7-siRNA/PJ34 markedly reduced the number of colonies formed by Hepa1-6 cells ($P<0.0001$), while PJ34, RBC-EVs/PJ34 or GalNac-RBC-EVs/PJ34 did not have any significant effects on the clonogenic potential of Hepa1-6 cells (all $P>0.05$, Figure 7B and C). Moreover, RBC-EVs/GalNac-Rab7-siRNA /PJ34 induced high rates of apoptosis compared with PJ34, RBC-EVs/PJ34 and GalNac-RBC-EVs/PJ34 (Figure 7D). In the in vivo HCC model, PJ34 (10 mg/kg) did not have any significant effects on tumor growth compared with the DMSO group ($P=0.76$). In contrast, RBC-EVs/PJ34 (5 mg/kg≈250 μg/kg PJ34) and GalNac-RBC-EV/PJ34 (5 mg/kg≈250 μg/kg PJ34) could inhibit tumor growth ($P=0.007$, $P=0.007$), and RBC-EVs/GalNac-Rab7-siRNA/PJ34 (5 mg/kg≈250 μg/kg PJ34) exhibited the highest therapeutic efficacy with maximum tumor inhibition compared to the other groups

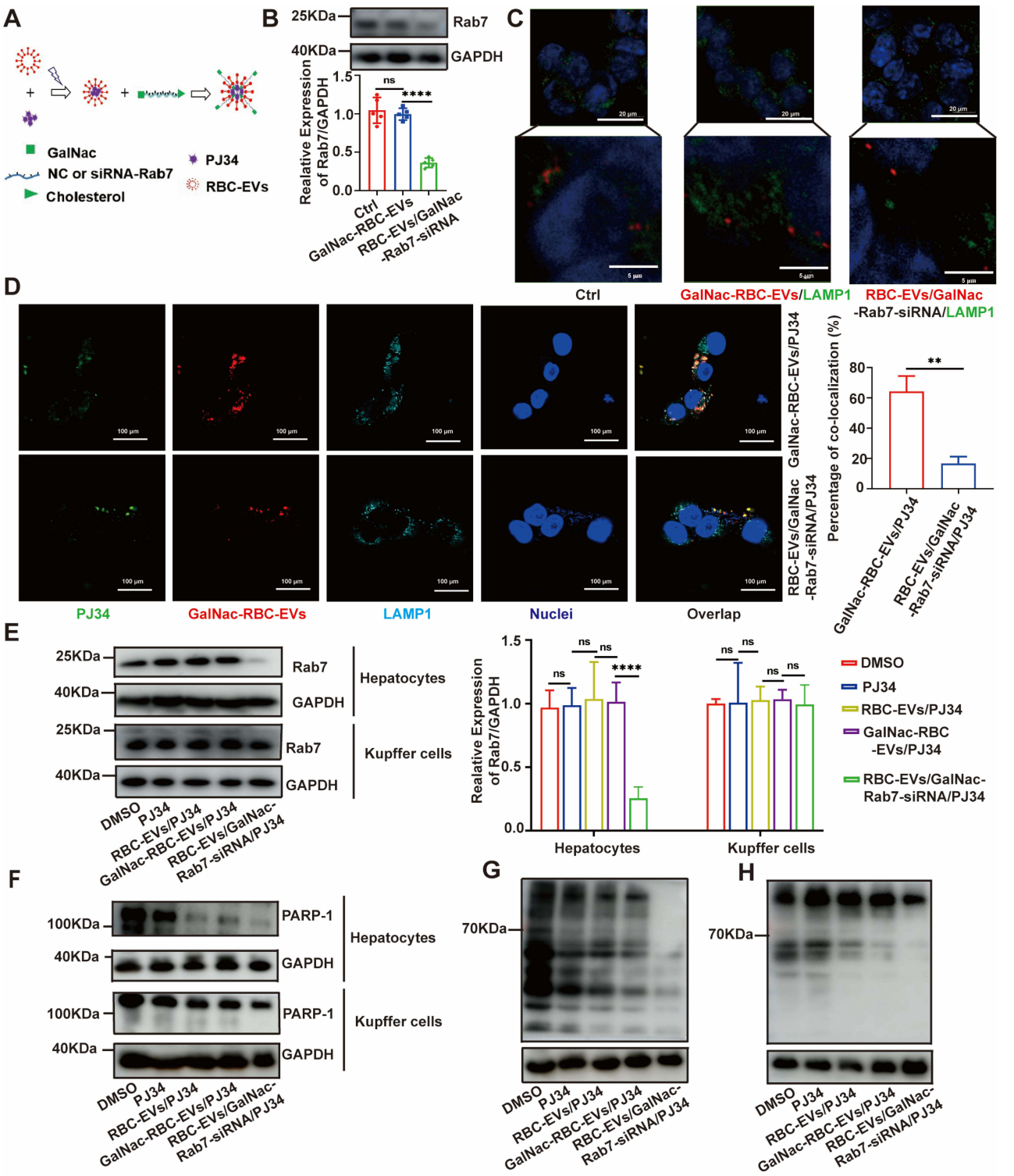

Figure 6 RBC-EVs/GalNac-Rab7-siRNA/PJ34 inhibited Rab7 and PARP-1 expression and activity in hepatocytes. (**A**) Schematic representation of loading PJ34 into GalNac-RBC-EVs or RBC-EVs/GalNac-siRNA-Rab7 via electroporation. (**B**) Immunoblot showing expression of Rab7 in Hepa1-6 cells treated with GalNac-RBC-EVs and RBC-EVs /GalNac-Rab7-siRNA. GAPDH was used as the internal control. Data are representative of three independent experiments. (**C**) Representative images of Hepa1-6 cells incubated with PKH26-labeled GalNac-RBC-EVs and RBC-EVs/GalNac-Rab7-siRNA showing co-localization of GalNac-RBC-EVs (red) with LAMP1 (green). (**D**) GalNac-RBC-EVs stained with PKH26 (red) were loaded with PJ34 (green) via electroporation, and then incubated with Hepa1-6 for 24 h. Representative images and percentage of the co-localization of GalNac-RBC-EVs/PJ34 with LAMP1 (cyan). (**E**) Immunoblot showing Rab7 expression in the hepatocytes and Kupffer cells. Data are representative of three independent experiments. (**F**) Immunoblot showing PARP-1 expression in the hepatocytes and Kupffer cells. (**G**) Immunoblot showing PAR expression in the hepatocytes. (**H**) Immunoblot showing PAR expression in the Kupffer cells. *P <0.05, **P <0.01, ***P <0.001 and ****P <0.0001 (one-way ANOVA test; mean ± SD).
Abbreviation: ns, no significant.

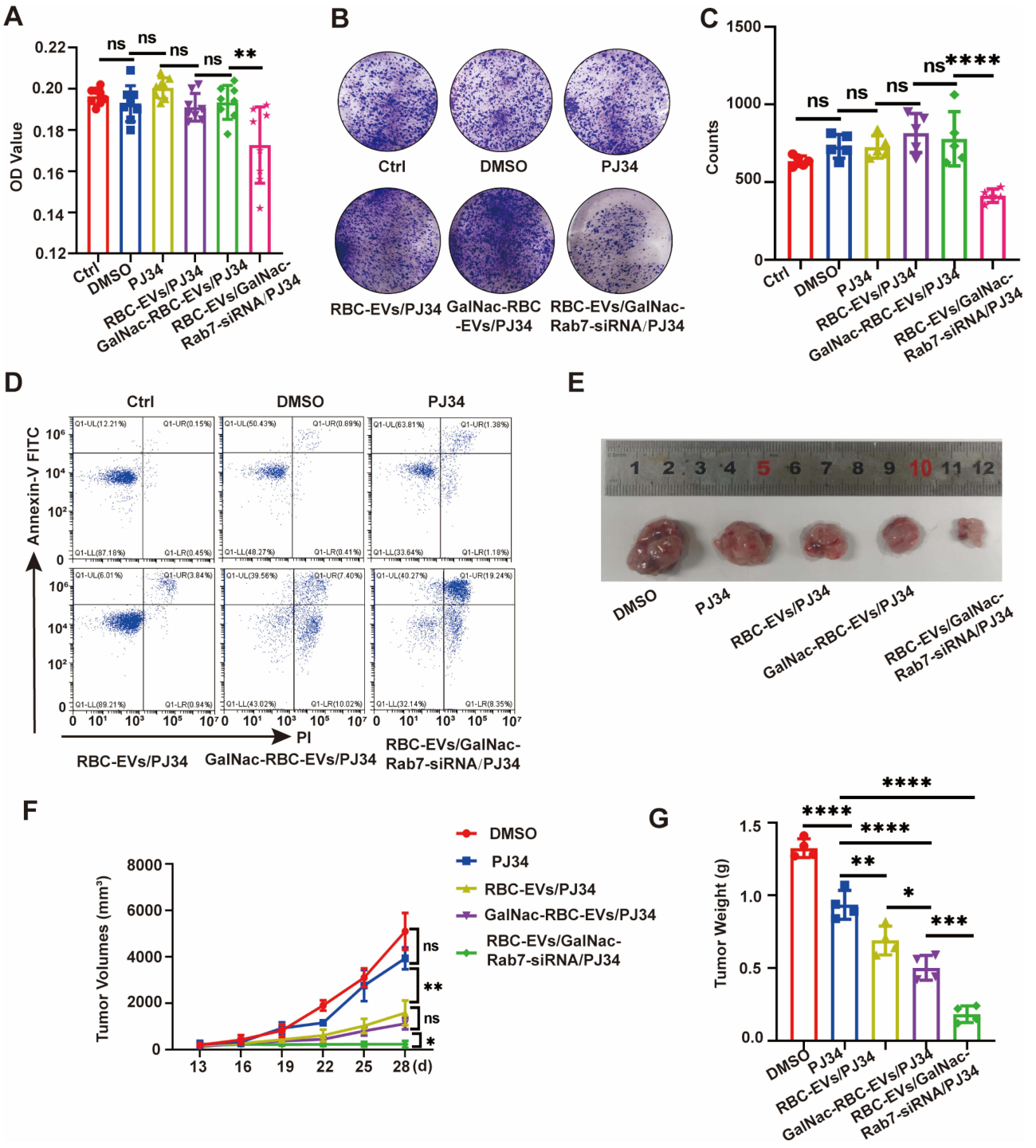

Figure 7 RBC-EVs/GalNac-Rab7-siRNA/PJ34 inhibited the progression of HCC in vitro and in vivo. (**A**) Viability of Hepa1-6 cells treated with DMSO, PJ34 (0.05 μg), RBC-EVs/PJ34 (1 μg), GalNac-RBC-EVs/PJ34 (1 μg) and RBC-EVs/GalNac-Rab7-siRNA/PJ34 (1 μg) for 48 h. (**B** and **C**) Number of colonies formed by Hepa1-6 cells in the DMSO, PJ34, RBC-EVs/PJ34, GalNac-RBC-EVs/PJ34 and RBC-EVs/GalNac-Rab7-siRNA/PJ34 groups. (**D**) Percentage of Annexin-V^+/PI^+ apoptotic Hepa1-6 cells in the DMSO, PJ34, RBC-EVs/PJ34, GalNac-RBC-EVs/PJ34 and RBC-EVs/GalNac-Rab7-siRNA/PJ34 groups. (**E**) Six-weeks-old female C57BL/6J mice were injected subcutaneously with Hepa1-6 cells (1×10^7 cells/mouse) at the right dorsal region, and treated with DMSO, PJ34 (10 mg/kg), RBC-EVs/PJ34 (5 mg/kg), GalNac-RBC-EVs/PJ34 (5 mg/kg) and RBC-EVs /GalNac-Rab7-siRNA/PJ34 (5 mg/kg). Representative images of the subcutaneous tumors are shown. (**F**) Tumor volumes in the indicated groups were measured every other day for 4 weeks (n=4). (**G**) Tumor weight in the indicated groups (n=4). *P <0.05, **P <0.01, ***P <0.001 and ****P <0.0001 (one-way ANOVA test; mean ± SD). **Abbreviation**: ns, no significant.

https://doi.org/10.2147/IJN.S510937

(Figure 7E, 7F and S4J). In addition, PJ34, RBC-EVs/PJ34 and GalNac-RBC-EVs/PJ34 reduced the tumor weight compared with the DMSO group (P=0.006, P<0.0001, P<0.0001), and RBC-EVs/GalNac-Rab7-siRNA/PJ34 led to the most significant reduction (Figure 7G). These findings suggest that RBC-EVs/GalNac-Rab7-siRNA/PJ34 is a promising drug for HCC treatment.

Drugs-Loaded GalNac-RBC-EVs Were Non-Toxic to Mice

RBC-EVs/GalNac-miR-155-ASO did not induce significant histopathological changes in the heart, liver, spleen, lungs and kidneys, quantitative histopathological scoring revealed no significant toxicity in the RBC-EVs/GalNac-miR-155-ASO group across all major organs compared to the control group (P > 0.05 for all organs) (Figure 8A). Additionally, there was no disruption observed in serum ALT and AST levels (all P > 0.05, Figure 8B), thereby indicating absence of any systemic toxicity. Chemotherapeutic drugs often result in adverse side effects due to their hydrophobicity and lack of targeting ability.[37] Therefore, we also tested the potential toxic effects of PJ34 and RBC-EVs/GalNac-Rab7-siRNA/PJ34 in healthy mice. As shown in Figure 8C, PJ34 induced a sharp decrease in the body weight of mice after 4 weeks of treatment (P=0.001), while no significant change occurred in the RBC-EVs/GalNac-Rab7-siRNA/PJ34 group (P=0.4). In detail, compared to the control group, food intake (Figure S4K) was reduced over a 28-day period in the PJ34 group (P=0.001). Additionally, a decrease in the activity of mice was observed in the PJ34 group. In contrast, both food intake and activity levels in the RBC-EVs/GalNac-Rab7-siRNA/PJ34 group were comparable to those of the control group. Although PARP-1 inhibitors are known to cause myelosuppression in patients during chemotherapy, the RBC, PLT and WBC counts were similar in the PJ34 and RBC-EVs/GalNac-Rab7-siRNA/PJ34 groups (Figure 8D). The lack of statistical significance may be attributable to the limited dataset available. The increase in ALT/AST levels was triggered by DMSO or PJ34 (P=0.03, P=0.005). However, no significant differences were observed in ALT and AST levels between the RBC-EVs/GalNac-Rab7-siRNA/PJ34 group and the PJ34 group (P=0.35, P=0.50, Figure 8E). Finally, neither PJ34 nor RBC-EVs/GalNac-Rab7-siRNA/PJ34 caused any pathological changes in the major organs, such as heart, liver, spleen, lungs and kidneys, quantitative histopathological scoring revealed no significant toxicity in the RBC-EVs/GalNac-Rab7-siRNA/PJ34 group across all major organs compared to the PJ34 group (P>0.05 for all organs) (Figure 8F). Overall, these data suggested that GalNac-RBC-EVs could mitigate the toxicity of the drug cargo, and potentially reduce adverse events.

Discussion

In this study, we have demonstrated that the conjugation of GalNac sequences to RBC-EVs facilitates the simultaneous delivery of siRNA/miRNA and chemical drugs into the hepatocytes, resulting in higher therapeutic efficacy in the treatment of ALF, NALFD and HCC.

RNA interference (RNAi)-based oligonucleotides, including siRNAs and miRNAs, have been extensively tested as therapeutic agents for various diseases. Due to their susceptibility to endogenous RNases, oligonucleotide drugs are often transported into target cells through a carrier. The covalent bonding of GalNac with chemically modified siRNAs yields a conjugate with nuclease stability compared to uncoupled siRNAs, leading to steady improvements in potency and duration of GalNac-siRNA conjugate activity.[38] Several GalNac-modified therapeutic siRNA and ASO are currently in the preclinical or clinical stages of testing.[39,40] However, many unresolved questions regarding the ASGPR/GalNac remain. For example, the saturation of ASGPR in high doses affecting the biodistribution in vivo should not be overlooked. Evidence showed that subcutaneously administered GalNac-siRNAs achieved better performances than intravenously administration. GalNac-siRNA would be rapidly eliminated by kidney filtration especially when administered intravenously.[41,42] Nonetheless, one study reported that a single dose of 10 mg/kg subcutaneous GalNac-siRNA showed 2-fold greater accumulation in kidney than liver.[43] In our present study, it is worth noting that the improvement effect of RBC-EVs/GalNac-miR-155-ASO on ALF was significantly different from that of GalNac-miR-155-ASO, in fact, the content of GalNac-miR-155-ASO carried by EVs was lower than that of the direct use of GalNac-miR-155-ASO. Therefore, when the same content of miRNA was used as a premise, GalNac-miR-155-ASO loaded with EVs has a stronger effect. We speculate that these results may be related to the elimination by kidney filtration after GalNac-miR-155-ASO administered intravenously, while GalNac sequences loaded with EVs accumulated mostly in liver, not in kidney.

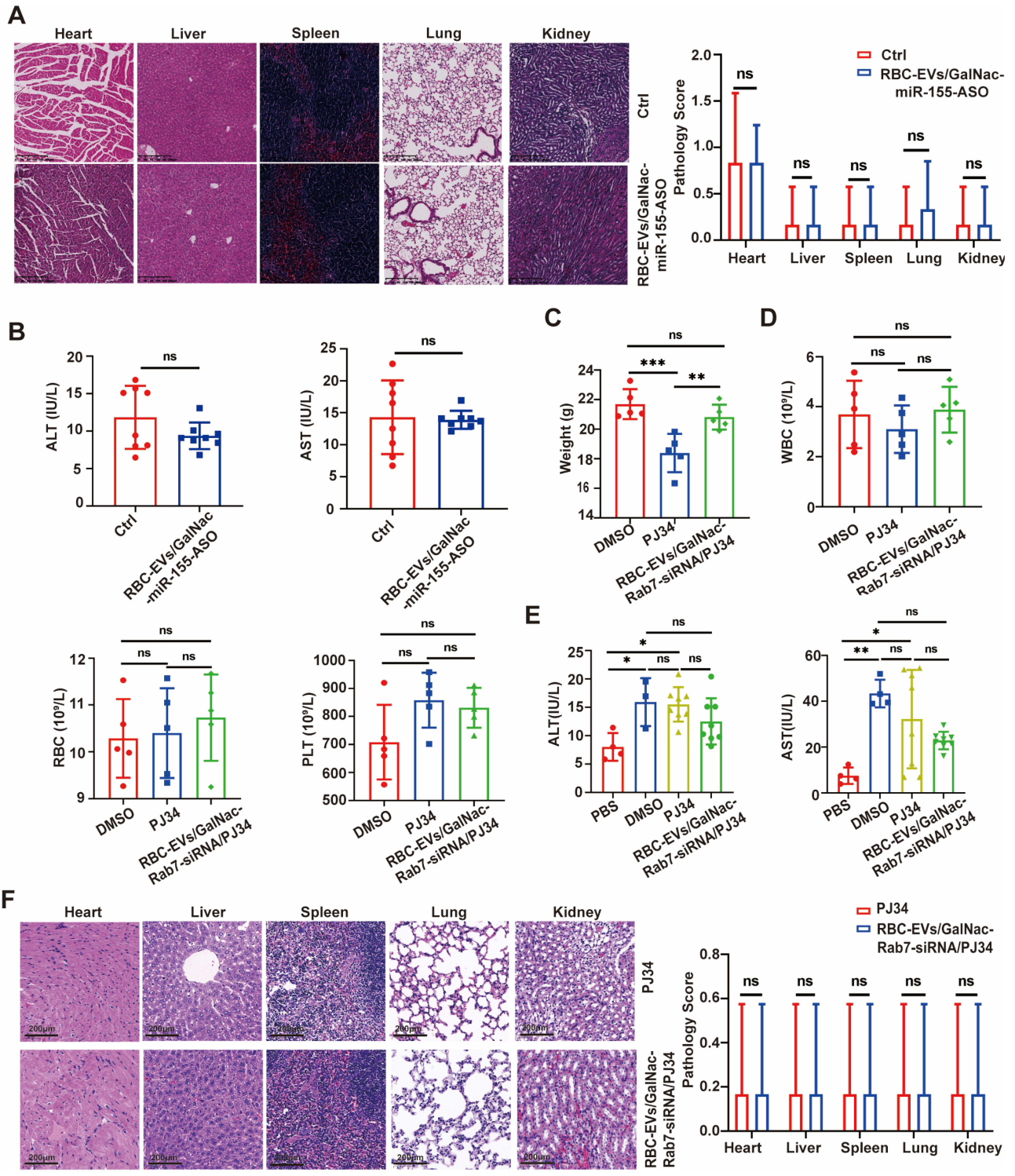

Figure 8 GalNac-RBC-EVs loaded with drugs had no significant adverse effects in mice. (**A**) Six-weeks-old C57BL/6J normal mice were intravenously injected with 5mg/kg RBC-EVs/GalNac-miR-155-ASO or PBS. The organs were harvested 24 h and stained with H&E. The representative images of H&E-stained heart, liver, spleen, lung and kidney and the histological scores in the RBC-EVs/GalNac-miR-155-ASO and Ctrl groups. Scale bars, 100 μm. (**B**) Serum ALT and AST levels in mice treated with RBC-EVs /GalNac-miR-155-ASO or PBS. (**C**) Six-weeks-old female C57BL/6J mice were intravenously injected with DMSO, PJ34 (10 mg/kg) and RBC-EVs/GalNac-Rab7-siRNA/PJ34 (5 mg/kg) every other day for 4 weeks. The body weight of the mice from the different groups are shown. (**D**) WBC, RBC and PLT counts in mice treated with DMSO, PJ34 and RBC-EVs/GalNac-Rab7-siRNA/PJ34. (**E**) Serum ALT and AST levels in mice treated with DMSO, PJ34 and RBC-EVs/GalNac-Rab7-siRNA/PJ34. (**F**) Representative images and the histological scores of H&E-stained sections of the heart, liver, spleen, lungs and kidneys from mice treated with PJ34 and RBC-EVs/GalNac-Rab7-siRNA/PJ34. Scale bars, 200 μm. **P* <0.05, ***P* <0.01, ****P* <0.001 and *****P* <0.0001 (one-way ANOVA test; mean ± SD).

Abbreviations: WBC, white blood cells; RBC, red blood cells; PLT, platelet, ALT, alanine transaminase; AST, aspartate aminotransferase; ns, no significant.

https://doi.org/10.2147/IJN.S510937

EVs can be modified with suitable ligands, such as aptamers and antibodies, to achieve targeted drug delivery.[44] ASGPR is a highly selective hepatocyte receptor that is abundantly expressed on the cell surface, and therefore can be potentially exploited as a shuttle for targeted drug delivery into hepatocytes.[45] For instance, compared to unmodified EVs, the EVs modified with cationized pullulan are more readily internalized by HepG2 cells through ASGPR in vitro, resulting in more significant therapeutic effects.[46] In our own study, the presence of GalNac sequences on the RBC-EVs facilitated their selective uptake into the hepatocytes via the ASGPR, which led to significant accumulation of the loaded cargos, such as miR-155-ASO or PJ34, in these cells. Targeted drug delivery can increase the concentration of drugs in specific cells, and reduce off-target toxicity induced by ubiquitous drug distribution, thereby improving the survival chances and quality of life of the patients. Zhang et al demonstrated that conjugation of GalNac sequences to atorvastatin enhanced the drug concentration in target cells, and relieved dose-related side effects like myopathy and muscle pain.[47] In our study, GalNac-RBC-EVs/PJ34 alleviated the symptoms of NAFLD and halted HCC progression more effectively compared to RBC-EVs/PJ34 or PJ34 by specifically targeting the hepatocytes. This improved NAFLD/HCC efficacy may attribute to higher local concentration of PJ34/siRNA in hepatocytes due to ASGPR targeting by reducing off-target effects. Furthermore, ASGPR internalization may bypass drug efflux pumps, overcoming chemoresistance.[48] Nevertheless, in vivo fluorescence imaging of the tumor-bearing mice showed similar accumulation of both unmodified and GalNac-modified RBC-EVs in the liver and tumor tissues, which may be attributed to the intricate network of hepatocytes, macrophages and extracellular matrix in the liver tumors.

The liver is composed of multiple cell types. In most instances, liver injury occurs because of immune-mediated or direct injury to the hepatocytes, then hepatocytes engage in cross-talk with multiple cellular subsets, such as infiltrating immune cells, resulting in release of pro-inflammatory signals and the activation of repair pathways.[49] Kupffer cells are a critical component of the immune system and are central to both the hepatic and systemic response to pathogens. In our previous study, we showed that the RBC-EV/miR-155-ASOs increased M2 but decreased M1 macrophages in livers of mice with ALF.[32] In this study, miR-155 expression in the Kupffer cells was also decreased in the RBC-EVs/GalNac-miR-155-ASO group, while GalNac-RBC-EVs primarily target hepatocytes. We acknowledge that Kupffer cells may capture a fraction of EVs due to their innate phagocytic activity,[50] in addition, hepatocytes treated with miR-155-ASO likely exhibit reduced pro-inflammatory cytokine secretion, which normally activate Kupffer cells via NF-κB signaling. This decreased inflammatory stimulation could downregulate miR-155 expression in Kupffer cells.

miR-155 plays a critical role in various physiological and pathological processes such as immunity, inflammation, and cancer. It is a central regulator of immune responses that is induced by inflammatory mediators.[51] Notably, miR-155 regulates multiple cell death pathways. In the context of pyroptosis, miR155-ASO modulates the components of the NLRP3 inflammasome, including NLRP3, ASC, and caspase-1, by inhibiting upstream regulators such as NF-κB. This intervention leads to a reduction in the cleavage of gasdermin D (GSDMD) and subsequently diminishes the release of pro-inflammatory cytokines, specifically IL-1β and IL-18.[52] In the context of apoptosis modulation, miR-155-ASO exerts its effects by downregulating pro-apoptotic genes, such as Bax, while concurrently upregulating anti-apoptotic factors, including Bcl-2. This regulatory mechanism is achieved through the inhibition of established miR-155 targets, such as SOCS6 and FOXO3a. Consequently, this modulation facilitates the equilibrium of mitochondrial permeability and the activation of caspases-3 and −7.[53,54] To suppress necroptosis, the inhibition of the miR-155-mediated activation of the RIPK1/RIPK3/MLKL signaling axis, for instance through targeting ZEB1 or SP1, results in the prevention of MLKL phosphorylation and subsequent membrane rupture by miR-155-ASO.[55] In our own study, we also found that down-regulating miR-155 via RBC-EVs/GalNac-miR-155-ASO inhibited multiple cell death involving apoptosis, pyroptosis, and necroptosis. A large literature indicates PANoptosis is a form of cell death that is highly connected to pyrolysis, apoptosis, and necrosis, and ZBP1 has been found to be essential for inducing PANoptosis.[56] Altogether, our results verified that down-regulating miR155 in liver not only alleviated pro-inflammatory response of ALF via macrophages polarization, but also mitigated multiple cell death of hepatocytes.

Many cell surface receptors and proteins are degraded within the lysosome and are affected by the MVB sorting pathway.[57] According to recent studies, the Rab7 protein controls the trafficking of endosomes/lysosomes and is vital for the biogenesis and functional maintenance of lysosomes.[58] A dominant negative Rab7 mutation can block cargo trafficking to the lysosomes.[59] In our research, to further optimise the therapeutic efficacy of PJ34, RBC-EVs/GalNac-

Rab7-siRNA was used to selectively knockdown of Rab7 in the hepatocytes. Rab7 silencing in the hepatocytes inhibited the fusion of RBC-EVs or GalNac-RBC-EVs/PJ34 with lysosomes, resulting in increased drug concentration and therapeutic effects. The enhanced efficacy of RBC-EVs/GalNac-Rab7-siRNA/PJ34 can be attributed to the spatial cooperation, wherein PJ34 targets the nuclei while Rab7-siRNA modulates endosomal activity, combined with temporal synergy, characterized by the induction of acute DNA damage alongside sustained modulation of trafficking pathways, we can exploit this kind of engineered RBC-EVs serving as feasible co-delivery nanosystem for hepatocyte-targeted, efficient transfection and gene/chemo combination therapy. We demonstrated that co-loading of chemical drugs and RNAs into one EV and co-delivering them into hepatocytes with superior accumulation remarkably inhibited the growth of the tumors and alleviating side effects. We acknowledge that systemic Rab7 inhibition could theoretically impair lysosomal function in other cell types. However, our GalNac-RBC-EV delivery system is designed to preferentially target hepatocytes via ASGPR-mediated uptake. Even in hepatocytes, Rab7 siRNA achieves partial rather than complete knockdown (Figure 6B), preserving basal lysosomal function for cellular homeostasis. In addition, other Rab GTPases (eg, Rab5, Rab9) may compensate for transient Rab7 suppression in non-target cells.[60] So it is improbable that the GalNac-Rab7-siRNA might result in unintended consequences.

Unlike synthetic carriers, RBC-EVs inherit the immune-privileged properties of parent RBCs, this natural advantages of RBC-EVs make them of greater clinical translational value. Nevertheless, it is imperative to consider potential regulatory and safety concerns associated with the utilization of RBC-EVs in human applications.[21] RBC-EVs have the potential to harbor latent viruses originating from donor RBCs, and factors such as donor age or storage conditions may influence the bioactivity of these EVs. There is also batch-to-batch variability in EV yield and purity, which can be attributed to the heterogeneity of donor RBCs. Furthermore, RBC-derived EVs may present "eat-me" signals, such as phosphatidylserine, that can prompt macrophage uptake. Additionally, there exists a risk of inducing a cytokine storm if EVs activate toll-like receptors.[61] In our study, GalNac-RBC-EVs mitigate the toxicity of the drug cargo, and reduced potential adverse events. GalNac modification enables ASGPR-mediated hepatocyte-specific uptake, thereby concentrating PJ34/siRNA in the liver and minimizing exposure to non-target organs where PJ34's PARP inhibition might cause myelosuppression.[62] Our biodistribution data (Figure S4F) show that GalNac-RBC-EVs significantly reduce drug accumulation in non-liver tissues. Additionally, RBC-EV's natural lipid bilayer shields PJ34 from premature degradation and nonspecific interactions with plasma proteins or healthy cells. This "stealth effect" reduces oxidative stress and inflammatory responses triggered by free PJ34. Our data demonstrate that EV-delivered PJ34 requires a lower dose than free PJ34 to achieve equivalent HCC inhibition (Figure 7F), directly reducing systemic toxicity. In our comprehensive 28-day investigation (Figure 8E), the administration of GalNac-RBC-EVs every other day at a dosage of 5 mg/kg did not result in any significant alterations in serum ALT/AST levels. Histopathological examination demonstrated normal architecture, with no evidence of fibrosis or inflammatory infiltration (Figure 8F). Additional research is required to evaluate chronic toxicity over a six-month duration in non-human primates and to assess the platform's efficacy in further liver models exhibiting impaired ASGPR expression.

Limitations and Future Directions

It is important to note that our strategy has several limitations that ought to be considered. First, in the context of clinical translational applications, large-scale isolation of EVs from donor RBCs necessitates the standardization of donor screening protocols and storage conditions. Additionally, measures to prevent EV aggregation during scale-up and sterility assessments extending beyond conventional endotoxin assays are essential. A significant number of GalNac sequences is necessary to thoroughly modify RBC-EVs and reduce their natural affinity for Kupffer cells. Although GalNac modification improves hepatocyte-specific delivery, the low-level expression of ASGPR in Kupffer cells or other non-parenchymal liver cells may result in unintended uptake. Current analyses confirm the targeting specificity and safety profile; however, future studies utilizing single-cell RNA sequencing will provide deeper insights into potential low-frequency off-target effects. Second, scalability of GMP-grade RBC-EV production and GalNac conjugation standardization require further optimization. Lastly, although RBC-EVs/GalNac-miR-155-ASO and GalNac-RBC-EVs/PJ34 specifically targeted the hepatocytes, some effects were also observed in the Kupffer cells. Therefore, the interactions

between hepatocytes and Kupffer cells in these disease models, along with the underlying mechanisms, warrant further investigation. This can be achieved through single-cell RNA sequencing (scRNA-seq) of liver tissues or the use of microfluidic liver-on-chip systems with separate chambers for hepatocytes and Kupffer cells to study paracrine effects. We underscore that such mechanistic insights are crucial for optimizing EV dosing to achieve a balance between hepatocyte targeting and Kupffer cell modulation.

Conclusion

The GalNac modification of RBC-EVs markedly improved hepatocyte-specific targeting, resulting in greater hepatic accumulation compared to unmodified EVs via ASGPR-mediated endocytosis. In ALF models, RBC-EVs/GalNAc-miR-155-ASO reduced inflammation through multi-model inhibition of hepatocyte death pathways. This included suppression of pyroptosis, as evidenced by decreased caspase-1 activity and reduced NLRP3 inflammasome activation; inhibition of apoptosis, indicated by a reduced Bax/Bcl-2 ratio and downregulation of cleaved caspase-3; and mitigation of necroptosis, demonstrated by decreased expression of RIPK3 and MLKL. These synergistic effects collectively preserved hepatocyte viability and diminished systemic inflammation. In the context of NAFLD, GalNac-RBC-EVs/PJ34 reduced hepatic triglyceride content and alleviated steatosis through PARP-1 inhibition. In HCC, RBC-EVs/GalNac-Rab7-siRNA/PJ34 inhibited tumor growth by utilizing Rab7 knockdown to extend PJ34 retention and enhance PARP-1 targeting. The platform's low immunogenicity and minimal off-target toxicity highlight its significant clinical potential. To progress towards clinical trials, it is imperative to undertake several key steps: conducting GLP-compliant toxicology studies in non-rodent species to assess dose-limiting toxicities, and standardizing EV production under GMP conditions with stringent batch consistency criteria. Building on these findings, future research will concentrate on validation in large-animal models, the exploration of GalNac-RBC-EVs for non-liver targets (such as ASGPR-positive pancreatic cancer) through the engineering of bispecific ligands, and the monitoring of EV-mediated epigenetic changes over the course of 12-month carcinogenicity studies. This research establishes GalNac-RBC-EVs as a versatile and clinically viable platform for precision liver therapy, combining endogenous biocompatibility with customizable targeting capabilities. Its modular design facilitates the treatment of multifactorial diseases through the simultaneous modulation of multiple pathways.

Data Sharing Statement

Data available on request from authors.

Ethics Statement

The animal experiments were approved by the animal care and use committee of Qilu Hospital of Shandong University (KYLL-2022(ZM)-001). The Animal Welfare and Ethics Committee of the hospital reviewed and approved all protocols, ensuring compliance with their operational guidelines for anesthesia, postoperative care, and euthanasia. The collection of human blood was conducted in accordance with the Declaration of Helsinki and approved by the local Ethical Committee and the Review Board of Qilu Hospital of Shandong University (KYLL-202310-037). All participants provided written informed consent.

Acknowledgments

This paper has been uploaded to ResearchSquare as a preprint: https://www.researchsquare.com/article/rs-3834825/v1.

Author Contributions

All authors made a significant contribution to the work reported, whether that is in the conception, study design, execution, acquisition of data, analysis and interpretation, or in all these areas; took part in drafting, revising or critically reviewing the article; gave final approval of the version to be published; have agreed on the journal to which the article has been submitted; and agree to be accountable for all aspects of the work.

Funding

This study was supported by the Shandong Provincial Natural Science Foundation (ZR2022QH046, ZR2020QH172, ZR2023YQ068), the National Natural Science Foundation of China (82300110, 82270086, 82072231, 82470068), and China International Medical Foundation (2021-N-15-26, Z-2017-24-2110).

Disclosure

The authors declare no conflicts of interest in this work.

References

1. Wang FS, Fan JG, Zhang Z, Gao B, Wang HY. The global burden of liver disease: the major impact of China. *Hepatology*. 2014;60(6):2099–2108. doi:10.1002/hep.27406
2. Gong J, Tu W, Liu J, Tian D. Hepatocytes: a key role in liver inflammation. *Front Immunol*. 2023;13:1083780. doi:10.3389/fimmu.2022.1083780
3. Wijdicks EFM. Hepatic Encephalopathy. *N Engl J Med*. 2017;376(2):186.
4. Engin A. Non-Alcoholic Fatty Liver Disease. *Adv Exp Med Biol*. 2017;960:443–467.
5. Sung H, Ferlay J, Siegel RL, et al. Global Cancer Statistics 2020: GLOBOCAN Estimates of Incidence and Mortality Worldwide for 36 Cancers in 185 Countries. *CA Cancer J Clin*. 2021;71(3):209–249. doi:10.3322/caac.21660
6. Song M, Cui X, Zhang J, et al. Shenlian extract attenuates myocardial ischaemia-reperfusion injury via inhibiting M1 macrophage polarization by silencing miR-155. *Pharm Biol*. 2022;60(1):2011–2024. doi:10.1080/13880209.2022.2117828
7. Ma Q, Huang S, Li MY, et al. Dihydromyricetin regulates the miR-155-5p/SIRT1/VDAC1 pathway to promote liver regeneration and improve alcohol-induced liver injury. *Phytomedicine*. 2025;139:156522. doi:10.1016/j.phymed.2025.156522
8. Wang S, Yang FJ, Shang LC, Zhang YH, Zhou Y, Shi XL. Puerarin protects against high-fat high-sucrose diet-induced non-alcoholic fatty liver disease by modulating PARP-1/PI3K/AKT signaling pathway and facilitating mitochondrial homeostasis. *Phytother Res*. 2019;33(9):2347–2359. doi:10.1002/ptr.6417
9. Ishteyaque S, Singh G, Yadav KS, et al. Cooperative STAT3-NFkB signaling modulates mitochondrial dysfunction and metabolic profiling in hepatocellular carcinoma. *Metabolism*. 2024;152:155771. doi:10.1016/j.metabol.2023.155771
10. Quiles-Perez R, Muñoz-Gámez JA, Ruiz-Extremera A, et al. Inhibition of poly adenosine diphosphate-ribose polymerase decreases hepatocellular carcinoma growth by modulation of tumor-related gene expression. *Hepatology*. 2010;51(1):255–266. doi:10.1002/hep.23249
11. Leng Y, Zhang Y, Cheng Y, et al. LIX1L aggravates MASH-HCC progression by reprogramming of hepatic metabolism and microenvironment via CD36. *Pharmacol Res*. 2025;211:107567. doi:10.1016/j.phrs.2024.107567
12. Huang S, Zhang B, Chen Y, et al. Poly(ADP-Ribose) Polymerase Inhibitor PJ34 Attenuated Hepatic Triglyceride Accumulation in Alcoholic Fatty Liver Disease in Mice. *J Pharmacol Exp Ther*. 2018;364(3):452–461. doi:10.1124/jpet.117.243105
13. Segel M, Lash B, Song J, et al. Mammalian retrovirus-like protein PEG10 packages its own mRNA and can be pseudotyped for mRNA delivery. *Science*. 2021;373(6557):882–889. doi:10.1126/science.abg6155
14. Dilliard SA, Cheng Q, Siegwart DJ. On the mechanism of tissue-specific mRNA delivery by selective organ targeting nanoparticles. *Proc Natl Acad Sci U S A*. 2021;118(52):e2109256118. doi:10.1073/pnas.2109256118
15. Zhou Y, Teng P, Montgomery NT, Li X, Tang W. Development of Triantennary N-Acetylgalactosamine Conjugates as Degraders for Extracellular Proteins. *ACS Cent Sci*. 2021;7(3):499–506. doi:10.1021/acscentsci.1c00146
16. Baenziger JU, Fiete D. Galactose and N-acetylgalactosamine-specific endocytosis of glycopeptides by isolated rat hepatocytes. *Cell*. 1980;22 (2):611–620. doi:10.1016/0092-8674(80)90371-2
17. Arbier-Torres L, Fortner KA, Iruzubieta P, et al. Silencing hepatic MCJ attenuates non-alcoholic fatty liver disease (NAFLD) by increasing mitochondrial fatty acid oxidation. *Nat Commun*. 2020;11(1):3360. doi:10.1038/s41467-020-16991-2
18. Prakash TP, Graham MJ, Yu J, et al. Targeted delivery of antisense oligonucleotides to hepatocytes using triantennary N -acetyl galactosamine improves potency 10-fold in mice. *Nucleic Acids Res*. 2014;42(13):8796–8807. doi:10.1093/nar/gku531
19. Gilleron J, Querbes W, Zeigerer A, et al. Image-based analysis of lipid nanoparticle-mediated siRNA delivery, intracellular trafficking and endosomal escape. *Nat Biotechnol*. 2013;31(7):638–646. doi:10.1038/nbt.2612
20. van Niel G, D'Angelo G, Raposo G. Shedding light on the cell biology of extracellular vesicles. *Nat Rev Mol Cell Biol*. 2018;19(4):213–228. doi:10.1038/nrm.2017.125
21. Elsharkasy OM, Nordin JZ, Hagey DW, et al. Extracellular vesicles as drug delivery systems: why and how? *Adv Drug Deliv Rev*. 2020;159:332–343. doi:10.1016/j.addr.2020.04.004
22. Ma SR, Xia HF, Gong P, Yu ZL. Red Blood Cell-Derived Extracellular Vesicles: an Overview of Current Research Progress, Challenges, and Opportunities. *Biomedicines*. 2023;11(10):2798. doi:10.3390/biomedicines11102798
23. Usman WM, Pham TC, Kwok YY, et al. Efficient RNA drug delivery using red blood cell extracellular vesicles. *Nat Commun*. 2018;9(1):2359. doi:10.1038/s41467-018-04791-8
24. Lu JW, Wang H, Yan-Li J, et al. Differential effects of pyrrolidine dithiocarbamate on TNF-alpha-mediated liver injury in two different models of fulminant hepatitis. *J Hepatol*. 2008;48(3):442–452. doi:10.1016/j.jhep.2007.10.014
25. Liu Y, Lou G, Li A, et al. AMSC-derived exosomes alleviate lipopolysaccharide/d-galactosamine-induced acute liver failure by miR-17-mediated reduction of TXNIP/NLRP3 inflammasome activation in macrophages. *EBioMedicine*. 2018;36:140–150. doi:10.1016/j.ebiom.2018.08.054
26. Li WC, Ralphs KL, Tosh D. Isolation and culture of adult mouse hepatocytes. *Methods Mol Biol*. 2010;633:185–196.
27. Chang W, Yang M, Song L, et al. Isolation and culture of hepatic stellate cells from mouse liver. *Acta Biochim Biophys Sin (Shanghai)*. 2014;46 (4):291–298. doi:10.1093/abbs/gmt143
28. Cheng KT, Xiong S, Ye Z, et al. Caspase-11-mediated endothelial pyroptosis underlies endotoxemia-induced lung injury. *J Clin Invest*. 2017;127 (11):4124–4135. doi:10.1172/JCI94495

29. Higaki I, Matsui-Yuasa I, Terakura M, Kinoshita H, Otani S. Increase in ornithine decarboxylase activity caused by hepatocyte growth factor in primary cultured adult rat hepatocytes. *Hepatology*. 1993;17(1):99–102. doi:10.1002/hep.1840170118
30. Li Z, Mao L, Yu B, et al. GB7 acetate, a galbulimima alkaloid from Galbulimima belgraveana, possesses anticancer effects in colorectal cancer cells. *J Pharm Anal*. 2022;12(2):339–349. doi:10.1016/j.jpha.2021.06.007
31. Ahn G, Banik SM, Miller CL, Riley NM, Cochran JR, Bertozzi CR. LYTACs that engage the asialoglycoprotein receptor for targeted protein degradation. *Nat Chem Biol*. 2021;17(9):937–946. doi:10.1038/s41589-021-00770-1
32. Zhang G, Huang X, Xiu H, et al. Extracellular vesicles: natural liver-accumulating drug delivery vehicles for the treatment of liver diseases. *J Extracell Vesicles*. 2020;10(2):e12030. doi:10.1002/jev2.12030
33. Li L, Fu J, Liu D, et al. Hepatocyte-specific Nrf2 deficiency mitigates high-fat diet-induced hepatic steatosis: involvement of reduced PPARγ expression. *Redox Biol*. 2020;30:101412. doi:10.1016/j.redox.2019.101412
34. Bai P, Cantó C. The role of PARP-1 and PARP-2 enzymes in metabolic regulation and disease. *Cell Metab*. 2012;16(3):290–295. doi:10.1016/j.cmet.2012.06.016
35. Gariani K, Ryu D, Menzies KJ, et al. Inhibiting poly ADP-ribosylation increases fatty acid oxidation and protects against fatty liver disease. *J Hepatol*. 2017;66(1):132–141. doi:10.1016/j.jhep.2016.08.024
36. Fei X, Li Z, Yang D, et al. Neddylation of Coro1a determines the fate of multivesicular bodies and biogenesis of extracellular vesicles. *J Extracell Vesicles*. 2021;10(12):e12153. doi:10.1002/jev2.12153
37. Gandhi S, Shende P. Cyclodextrins-modified metallic nanoparticles for effective cancer therapy. *J Control Release*. 2021;339:41–50. doi:10.1016/j.jconrel.2021.09.025
38. Springer AD, Dowdy SF. GalNAc-siRNA Conjugates: leading the Way for Delivery of RNAi Therapeutics. *Nucleic Acid Ther*. 2018;28(3):109–118. doi:10.1089/nat.2018.0736
39. Glazier DA, Liao J, Roberts BL, et al. Chemical Synthesis and Biological Application of Modified Oligonucleotides. *Bioconjug Chem*. 2020;31(5):1213–1233. doi:10.1021/acs.bioconjchem.0c00060
40. Huang Y. Preclinical and Clinical Advances of GalNAc-Decorated Nucleic Acid Therapeutics. *Mol Ther Nucleic Acids*. 2017;6:116–132. doi:10.1016/j.omtn.2016.12.003
41. Hu B, Zhong L, Weng Y, et al. Therapeutic siRNA: state of the art. *Signal Transduct Target Ther*. 2020;5(1):101. doi:10.1038/s41392-020-0207-x
42. Godinho BMDC, Knox EG, Hildebrand S, et al. PK-modifying anchors significantly alter clearance kinetics, tissue distribution, and efficacy of therapeutics siRNAs. *Mol Ther Nucleic Acids*. 2022;29:116–132. doi:10.1016/j.omtn.2022.06.005
43. Rider D, Chivers S, Aretz J, et al. Preclinical Toxicological Assessment of A Novel siRNA, SLN360, Targeting Elevated Lipoprotein (a) in Cardiovascular Disease. *Toxicol Sci*. 2022;189(2):237–249. doi:10.1093/toxsci/kfac067
44. Luo ZW, Fx L, Yw L, et al. Aptamer-functionalized exosomes from bone marrow stromal cells target bone to promote bone regeneration. *Nanoscale*. 2019;11(43):20884–20892. doi:10.1039/C9NR02791B
45. Bon C, Hofer T, Bousquet-Mélou A, Davies MR, Krippendorff BF. Capacity limits of asialoglycoprotein receptor-mediated liver targeting. *MAbs*. 2017;9(8):1360–1369. doi:10.1080/19420862.2017.1373924
46. Ellipilli S, Wang H, Binzel DW, Shu D, Guo P. Ligand-displaying-exosomes using RNA nanotechnology for targeted delivery of multi-specific drugs for liver cancer regression. *Nanomedicine*. 2023;50:102667. doi:10.1016/j.nano.2023.102667
47. Zhang Y, Zhang X, Zeng C, et al. Targeted delivery of atorvastatin via asialoglycoprotein receptor (ASGPR). *Bioorg Med Chem*. 2019;27(11):2187–2191. doi:10.1016/j.bmc.2019.04.019
48. Tang W, Chen Z, Zhang W, et al. The mechanisms of sorafenib resistance in hepatocellular carcinoma: theoretical basis and therapeutic aspects. *Signal Transduct Target Ther*. 2020;5(1):87. doi:10.1038/s41392-020-0187-x
49. Tu T, Calabro SR, Lee A, et al. Hepatocytes in liver injury: victim, bystander, or accomplice in progressive fibrosis? *J Gastroenterol Hepatol*. 2015;30(12):1696–1704. doi:10.1111/jgh.13065
50. Jayasinghe MK, Pirisinu M, Yang Y, et al. Surface-engineered extracellular vesicles for targeted delivery of therapeutic RNAs and peptides for cancer therapy. *Theranostics*. 2022;12(7):3288–3315. doi:10.7150/thno.68667
51. Elton TS, Selemon H, Elton SM, Parinandi NL. Regulation of the MIR155 host gene in physiological and pathological processes. *Gene*. 2013;532(1):1–12. doi:10.1016/j.gene.2012.12.009
52. Li G, Xiu L, Li X, Ma L, Zhou J. miR-155 inhibits chondrocyte pyroptosis in knee osteoarthritis by targeting SMAD2 and inhibiting the NLRP3/Caspase-1 pathway. *J Orthop Surg Res*. 2022;17(1):48. doi:10.1186/s13018-021-02886-5
53. Li Y, Sun W, Saaoud F, et al. MiR155 modulates vascular calcification by regulating Akt-FOXO3a signalling and apoptosis in vascular smooth muscle cells. *J Cell Mol Med*. 2021;25(1):535–548. doi:10.1111/jcmm.16107
54. Shen R, Wang Y, Cx W, et al. MiRNA-155 mediates TAM resistance by modulating SOCS6-STAT3 signalling pathway in breast cancer. *Am J Transl Res*. 2015;7(10):2115–2126.
55. Prasad Panda S, Kesharwani A, Prasanna Mallick S, Prasanth D, Kumar Pasala P, Bharadwaj Tatipamula V. Viral-induced neuronal necroptosis: detrimental to brain function and regulation by necroptosis inhibitors. *Biochem Pharmacol*. 2023;213:115591. doi:10.1016/j.bcp.2023.115591
56. Hao Y, Yang B, Yang J, et al. ZBP1: a Powerful Innate Immune Sensor and Double-Edged Sword in Host Immunity. *Int J Mol Sci*. 2022;23(18):10224. doi:10.3390/ijms231810224
57. Piper RC, Katzmann DJ. Biogenesis and function of multivesicular bodies. *Annu Rev Cell Dev Biol*. 2007;23(1):519–547. doi:10.1146/annurev.cellbio.23.090506.123319
58. Bucci C, Thomsen P, Nicoziani P, McCarthy J, van Deurs B. Rab7: a key to lysosome biogenesis. *Mol Biol Cell*. 2000;11(2):467–480. doi:10.1091/mbc.11.2.467
59. Guerra F, Bucci C. Multiple Roles of the Small GTPase Rab7. *Cells*. 2016;5(3):34. doi:10.3390/cells5030034
60. Gillingham AK, Sinka R, Torres IL, Lilley KS, Munro S. Toward a comprehensive map of the effectors of rab GTPases. *Dev Cell*. 2014;31(3):358–373. doi:10.1016/j.devcel.2014.10.007
61. Thangaraju K, Neerukonda SN, Katneni U, Buehler PW. Extracellular Vesicles from Red Blood Cells and Their Evolving Roles in Health, Coagulopathy and Therapy. *Int J Mol Sci*. 2020;22(1):153. doi:10.3390/ijms22010153
62. Negi P, Lakshmanan K, Patel PK, Rajagopal K, Byran G. An Update on Poly(ADP-ribose) Polymerase I-A Brief Review. *Mini Rev Med Chem*. 2023;23(18):1762–1771. doi:10.2174/1389557523666230221145844